Vibrational modes of a thin sheet in a pressurized chamber

Oz Oshri [*]
Department of Mechanical Engineering, Ben-Gurion University of the Negev, Beer-Sheva 84105, Israel

(Received 25 April 2024; accepted 7 January 2025; published 31 January 2025)

We investigate the intricate dynamics arising from the vibrations of a thin sheet in a compressible fluid medium. The system comprises a closed chamber that is filled with an ideal gas and is divided into two parts by a thin sheet. We develop an analytical model that combines the elasticity of thin sheets with the hydrodynamics of compressible fluids to analyze how the sheet's material properties and compression affect the system's lowest mode of vibration. We employ a linear stability analysis around three distinct solutions of the static equations and show that the lowest mode consists of either a vortexlike patterned flow that is localized around the area of the sheet or an extended, oscillating net flow. While these eigenmodes are influenced mainly by the ratio between the thermal energy of the fluid and the bending rigidity of the sheet, the frequency of the vibrations also depends on the mass ratio between the sheet and the fluid. Notably, our findings can provide guidelines for the design of technological applications that require precise control over elastohydrodynamic interactions.

DOI: 10.1103/PhysRevFluids.10.013905

I. INTRODUCTION

The intricate dynamics between thin sheets and compressible fluids plays a pivotal role in many microelectromechanical systems and microfluidic switches, which require precise control over fluid dynamics and structural movement. For example, in accelerometers, thin silicon membranes "sense" acceleration by interacting with gases [1,2], while in lab-on-a-chip devices, flexible membranes regulate fluid flow within microchannels [3,4]. In addition, vibrating thin sheets in air are instrumental in energy harvesting [5,6] by facilitating the transformation of mechanical vibrations into electrical energy [7]. In yet another important application, thin sheets are incorporated into sound sensors, where they convert acoustic waves into electrical signals for various sensing purposes [8,9].

In recent publications [10,11], we presented a new configuration that relies on such a fluid-structure interaction, namely, a rectangular chamber, with a movable piston, that is divided into two parts by a thin sheet [see Fig. 1(a)]. The two compartments of the chamber are assumed to be filled with an ideal gas and are initially set to the same thermodynamic state. When the piston is moved inwards quasistatically, it compresses the sheet, which may, in general, buckle. This buckling induces inhomogeneity between the upper and lower parts of the chamber [Fig. 1(b)], which depends on the magnitude of the compression and the ratio between the thermal energy of the gas and the bending rigidity of the sheet. In the presence of this inhomogeneity, the system accumulates additional energy—beyond that of such a system without a dividing sheet—which scales with the bending energy of the sheet. One approach to harness this extra energy is to allow the fluid to flow from one part of the chamber into the other part, as explored in previous work [12,13]. In this scenario, the sheet is restored to its minimum energetic state by spontaneous release of its stored bending energy into the flow. We emphasize that, while the geometry considered in our analysis

[*]Contact author: oshrioz@bgu.ac.il

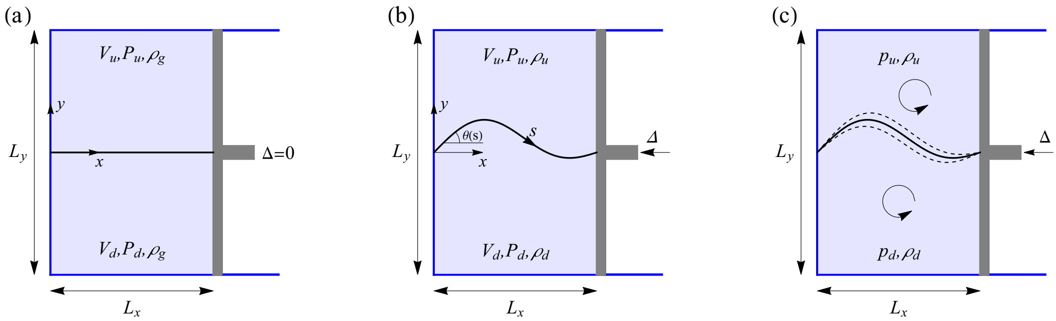

FIG. 1. Schematic illustration of the problem. A thin sheet divides a closed rectangular chamber of dimensions $L_x \times L_y \times W$ into two parts (the W dimension is perpendicular to the xy plane). (a) When $\Delta = 0$ ($L = L_x$), the gases above and below the sheet are in identical states; i.e., the volumes $V_\mathrm{u} = V_\mathrm{d} = L_x L_y W/2$, the density $\rho_\mathrm{g} = m_\mathrm{g}/V_\mathrm{u}$, and the pressures $P_\mathrm{u} = P_\mathrm{d}$ are all equal. (b) When $\Delta > 0$, the sheet buckles and induces some inhomogeneity between the upper and lower parts of the chamber. Under quasistatic conditions, the gas remains homogeneous in each part of the chamber, i.e., V_i, P_i, and ρ_i ($i = \mathrm{u, d}$) are all constants. (c) Once the system is perturbed dynamically, the fluid and the sheet are set in motion, and the hydrodynamic and elastic fields depend on both space and time.

is simplified to highlight fundamental mechanisms, practical applications may employ alternative configurations of the sheet and chamber, as discussed, for example, in Ref. [14].

Although the amount of this energy is relatively small, since the bending energy scales with the thickness of the sheet cubed, certain applications specifically rely on this precise but modest energy increase. Examples include micromechanical switches in soft robotics [15,16] and micropumps that are designed for delivering small-scale particles, such as a single red blood cell [17–19]. Furthermore, external energy sources, such as winds, ocean waves, and acoustic vibrations, can be harvested by deforming thin solid objects. This deformation is then converted into electric power by exploiting the piezoelectric effect [20,21]. To efficiently collect energy from the environment, it is advantageous to design the system close to resonance, where the frequency of the external source aligns with the natural frequency of the system. The natural frequency of the system in our setup depends not only on the material properties of the sheet itself but also on the properties of the fluid and the chamber's dimensions. This increases the flexibility of tuning the system's natural frequency.

Motivated by these applications, in this paper we study the elastohydrodynamic interaction resulting from small dynamic perturbations of the above-described system. In particular, we investigate how the lowest natural frequency of the system depends on the lateral displacement Δ, the thermal-to-bending energy ratio η, the sheet-to-fluid mass ratio λ, and the dimensions of the chamber. To this end, we formulate an analytical model that combines the elasticity of thin sheets with the hydrodynamic theory of compressible fluids. First, we study the quasistatic evolution of the system and show that it consists of three distinct branches of solutions: (i) a symmetric branch, where the bending energy of the sheet dominates over the energy of the gas, which leads to a symmetric configuration of the sheet similar to that observed in the first mode of buckling; (ii) an asymmetric branch, where the energy of the gas exceeds the bending energy of the sheet, leading to an asymmetric configuration, similar to that observed in the second mode of buckling; and (iii) a narrow transition region between the symmetric and the asymmetric branches, where the sheet lacks a specific symmetry. We perform a linear stability analysis around each of these branches and explore how the deformation of the sheet is coupled to the motion of the fluid and how this coupling affects the lowest frequency.

While the general dynamical formulation of the problem yields a system of intractable and nonlinear equations, we employ the small-amplitude approximation along with modal expansion of the elastic and hydrodynamic fields to simplify the equations into tractable forms. This approach enables us to elucidate the underlying physical mechanisms governing the collective motion of the sheet and the fluid. Specifically, we observe a vortexlike patterned flow localized around the sheet in the symmetric branch. The degree of localization is found to scale with the total length of the sheet and is influenced mainly by the thermal-to-bending energy ratio. In contrast, oscillations in the asymmetric branch exhibit an extended flow pattern near the critical point at which this branch stabilizes. However, as the thermal-to-bending energy ratio increases, the system behaves as if the fluid is incompressible, leading, once again, to localized vibrations. Analytical solutions for the lowest frequency are derived for each scenario. Furthermore, we demonstrate that, in the limit of a small lateral compression, the frequency remains largely independent of this compression both in the symmetric and the asymmetric branches. However, in the transition region, the lowest frequency follows a power-law dependence on the magnitude of the lateral compression.

The paper is organized as follows: In Sec. II, we formulate the problem and recap some of the main results regarding the quasistatic evolution of the system. Then, in Sec. III, we introduce the small-amplitude approximation and the modal expansion. In Sec. IV, we describe the linear stability analysis of the reduced formulation. Lastly, in Sec. V, we summarize our main results and discuss possible extensions for future studies.

II. FORMULATION OF THE PROBLEM

A thin and inextensible sheet of length L, bending modulus B, thickness h, and density ρ_{sh} divides a closed rectangular chamber into two parts, as depicted in Fig. 1(a). The length, height, and width dimensions of the chamber are denoted by L_x, L_y, and W, respectively. A Cartesian coordinate system is placed on the left edge of the sheet. The volumes of the chamber above and below the sheet, V_{u} and V_{d}, are filled with an ideal gas of total mass m_{g} and temperature T. Hereafter, the subscripts "u" and "d" are used to denote quantities that are related to the upper and lower parts of the chamber, respectively. When the piston is moved inwards, the sidewall of the chamber is quasistatically displaced by $\Delta = L - L_x$, which induces buckling of the sheet, as illustrated in Fig. 1(b). This buckling, in general, introduces inhomogeneity within the chamber, which alters the volumes and, consequently, the pressures in each side of the chamber. We denote these quasistatic pressures by P_{u} and P_{d}. Lastly, the system is dynamically perturbed around the quasistatic state, as depicted schematically in Fig. 1(c).

Given the physical parameters of the sheet (L, B, h, ρ_{sh}), the chamber's dimensions (L_x, L_y, W), and the properties of the fluid (temperature T and density ρ_{g}), our objective is to determine the stable quasistatic solution of the system, along with its lowest mode of vibration.

In the following analysis, we normalize all lengths to the total length of the sheet, L, time by the inertial timescale of the sheet, $L^2\sqrt{\rho_{\mathrm{sh}}h/B}$, and the density of the fluid by its density when $\Delta = 0$, i.e., $\rho_{\mathrm{g}} = 2m_{\mathrm{g}}/(L_xL_yW)$. This normalization implies the normalization of the elastic and the hydrodynamic fields, as is further emphasized during the formulation.

Our analysis relies on the following five assumptions. First, we assume an isothermal system, where the temperature remains constant at all times. Second, we assume that the volume of the sheet is negligible compared to the volume of the chamber, such that $V_{\mathrm{u}}(t) + V_{\mathrm{d}}(t) = L_xL_yW$. Third, we assume that the sheet deforms only in the xy plane and remains flat along the spanwise direction; i.e., the sheet remains flat along the z axis. Therefore, we set $W = 1$ and consider a two-dimensional system. Fourth, we assume that there is no contact between the sheet and the sidewalls of the chamber, or of the sheet with itself throughout the evolution of the system. Fifth, we assume that the maximum amplitude of the sheet is always much smaller than the height of the chamber.

The state of a compressible and irrotational inviscid fluid is determined by three hydrodynamic fields. The first two are the pressure and density fields $p_i(x, y, t)$ and $\rho_i(x, y, t)$, respectively, and the third field is the potential function $\phi_i(x, y, t)$, from which we can determine the fluid's velocity by $\mathbf{v}_i = \nabla\phi_i$, where ∇ is the two-dimensional gradient operator. Following our normalization convention, it can be shown that the pressures and the hydrodynamic potentials are normalized by B/L^3 and $(B/\rho_{\mathrm{sh}}h)^{1/2}$, respectively. The evolution of the above fields in space and over time is determined by the equation of state of the ideal gas, the continuity equation, and Bernoulli's equation [22]:

$$p_i = \eta\rho_i, \tag{1a}$$

$$\frac{D\rho_i}{Dt} + \rho_i\nabla^2\phi_i = 0, \tag{1b}$$

$$\lambda\eta\ln\rho_i + \frac{\partial\phi_i}{\partial t} + \frac{1}{2}|\nabla\phi_i|^2 = c_i(t), \tag{1c}$$

where $i = \mathrm{u}, \mathrm{d}$ and $c_i(t)$ are arbitrary time-dependent constants. In the following analysis, we set $c_i(t) = \lambda\eta\ln(P_i/\eta)$, where P_i/η are the densities of the gas in the static solution. With this choice, Bernoulli's equation is automatically satisfied when the flow fields vanish. In addition, we define the following dimensionless parameters:

$$\eta = \frac{\rho_{\mathrm{g}}RTL^3}{B}, \quad \lambda = \frac{\rho_{\mathrm{sh}}h}{\rho_{\mathrm{g}}L}, \quad \Delta = \frac{L - L_x}{L}, \tag{2}$$

where R is the specific gas constant. The parameter η is the ratio between the thermal energy of the gas and the bending rigidity of the sheet, the parameter λ is the sheet-to-fluid mass ratio, and the parameter Δ is the lateral displacement of the sheet. These parameters, in addition to L_y, determine the system's setup.

To close the system of equations, we specify the boundary conditions at the fluid-chamber and the fluid-sheet interfaces. For this purpose, we first prescribe a no-penetration condition at all the fluid-chamber interfaces:

$$\frac{\partial\phi_i}{\partial x}(0, y, t) = \frac{\partial\phi_i}{\partial x}(1 - \Delta, y, t) = 0, \tag{3a}$$

$$\frac{\partial\phi_{\mathrm{u}}}{\partial y}(x, L_y/2, t) = \frac{\partial\phi_{\mathrm{d}}}{\partial y}(x, -L_y/2, t) = 0. \tag{3b}$$

To model the interaction between the sheet and the fluid, we define the position vector to a point on the sheet by $\mathbf{x}_{\mathrm{sh}} = (x_{\mathrm{sh}}(s, t), y_{\mathrm{sh}}(s, t))$ and the angle $\theta(s, t)$ between the tangent to the sheet and the x axis [see Fig. 1(b)], where $s \in [0, 1]$ is the normalized arclength parameter on the sheet. These three elastic fields are related by the following geometric constraints:

$$\frac{\partial x_{\mathrm{sh}}}{\partial s} = \cos\theta, \tag{4a}$$

$$\frac{\partial y_{\mathrm{sh}}}{\partial s} = \sin\theta. \tag{4b}$$

Using these definitions, we impose the kinematic boundary conditions on each side of the fluid-sheet interfaces by

$$x = x_{\mathrm{sh}}(s, t) \;\; y = y_{\mathrm{sh}}(s, t): \quad \hat{\mathbf{n}}_i \cdot \frac{\partial\mathbf{x}_{\mathrm{sh}}}{\partial t} = \hat{\mathbf{n}}_i \cdot \nabla\phi_i, \tag{5}$$

where $\hat{\mathbf{n}}_{\mathrm{d}} = (-\sin\theta, \cos\theta)$ and $\hat{\mathbf{n}}_{\mathrm{u}} = (\sin\theta, -\cos\theta)$ are the outward unit normal vectors to the enclosed volume. Additionally, we need to ensure proper transfer of momentum between the sheet and the fluid. This requirement is met by the following balance of moments and forces on the sheet:

$$\frac{\partial^2\theta}{\partial s^2} = -F_x\sin\theta + F_y\cos\theta, \tag{6a}$$

$$\frac{\partial^2\mathbf{x}_{\mathrm{sh}}}{\partial t^2} = -\frac{\partial\mathbf{F}}{\partial s} + [p_{\mathrm{d}}(x_{\mathrm{sh}}, y_{\mathrm{sh}}, t) - p_{\mathrm{u}}(x_{\mathrm{sh}}, y_{\mathrm{sh}}, t)]\hat{\mathbf{n}}_{\mathrm{d}}, \tag{6b}$$

where $\mathbf{F} = (F_x(s,t), F_y(s,t))$ is the vector of the reaction forces per unit length in the sheet, and the hydrodynamic pressures in Eq. (6b) are calculated on the sheet-fluid interfaces. Equations (6) are supplemented by the following boundary conditions at the sheet edges:

$$x_{\text{sh}}(0,t) = 0, \quad x_{\text{sh}}(1,t) = 1 - \Delta, \tag{7a}$$

$$y_{\text{sh}}(0,t) = 0, \quad y_{\text{sh}}(1,t) = 0, \tag{7b}$$

$$\frac{\partial \theta}{\partial s}(0,t) = 0, \quad \frac{\partial \theta}{\partial s}(1,t) = 0, \tag{7c}$$

where we assume hinged boundary conditions in Eq. (7c).

This completes the formulation of the problem. In summary, given the thermal-to-bending ratio η, the sheet-to-fluid mass ratio λ, the lateral displacement Δ, the vertical dimension of the chamber, L_y, and an appropriate set of initial conditions, we can determine the evolution of the system from the solution of the coupled equations, Eqs. (1)–(7).

However, the focus of this paper is not on exploring general solutions of the problem, but rather on exploring the linear stability of the system in the vicinity of a specific static equilibrium configuration. To achieve this aim, we first must investigate the static solutions of the model. This investigation was carried out in Ref. [10], and for completeness, we recap the main results in the next section. Second, we need to expand Eqs. (1)–(7) around their respective base solutions and to derive a set of linear equations that govern the evolution of the small perturbations. This conventional procedure is detailed in Appendix A, with the corresponding numerical solutions presented later in the analysis.

Finally, to gain a deeper understanding of the physical behavior of the system and to make analytical progress, we find it instructive to simplify the above formulation by using the small-amplitude approximation, and then to perform a linear stability analysis around this reduced model. The details of this reduction are elaborated upon in a subsequent section.

A. Recap of the quasistatic solution

Our system of Eqs. (1)–(7) has a conserved first integral that corresponds to the total free energy of the system (see derivation in Appendix B). In the quasistatic problem, this free energy reduces to

$$E = \frac{1}{2}\int_0^1 \left(\frac{d\theta}{ds}\right)^2 ds - \frac{\eta L_x L_y}{2}(\ln V_{\text{u}} + \ln V_{\text{d}}), \tag{8}$$

where the first term on the right-hand side of Eq. (8) corresponds to the bending energy of the sheet, and the second term to the Helmholtz free energy of the gas. The minimization of this energy, given the geometric constraints, Eq. (4), and the boundary conditions at the sheet's ends, Eq. (7), yield the force balance equations, Eq. (6), without the inertial term. Clearly, the quasistatic solution depends only on three out of the four dimensionless numbers: the excess length Δ, the parameter η, and the vertical dimension of the chamber, L_y. The static solution does not account for the sheet-to-fluid mass ratio, since it originates from the inertia of the sheet and the fluid.

In an earlier publication [10], we demonstrated that the quasistatic solution consists of three distinct branches of solutions that arise from the energetic competition between the sheet and the fluid. The first branch corresponds to symmetric configurations of the sheet around the chamber's midaxis, and is therefore referred to as the "symmetric branch." In this branch, the bending energy of the sheet dominates over the energy of the fluid ($\eta \ll 1$), and the sheet exhibits a configuration that closely resembles the first mode of buckling, as one would expect from the minimization of bending energy alone. This buckling pattern leads to asymmetry between the upper and lower volumes in the chamber and consequently gives rise to a nonzero pressure difference. In the following analysis, we always assume that the sheet buckles upwards, such that $P_{\text{ud}} > 0$. Since the system has mirror symmetry around the x axis, the downwards solutions, with $P_{\text{ud}} < 0$, are obtained by a reflection of the elastic shapes around the horizontal axis.

The second branch corresponds to asymmetric configurations of the sheet around the chamber's midaxis and is therefore referred to as the "asymmetric branch." In this scenario, the energy of the gas dominates over the bending energy of the sheet ($\eta \gg 1$), and the sheet exhibits the second mode of buckling, as expected from the minimization of the fluid's energy alone. In this state, the system maintains equal volumes in the two parts of the chamber, and, as a result, equal pressures above and below the sheet ($P_{\rm ud} = 0$). Finally, there exists a transition region between these two branches, where the sheet lacks a distinct symmetry and experiences a gradual shape transition from a symmetric to an asymmetric configuration. As a result, the pressure difference continuously decreases to zero.

In Ref. [10], we demonstrated that, upon expanding the theory to the leading order in the sheet's amplitude ($\Delta \ll 1$), only the first two branches, symmetric and asymmetric, appear stable, while the branch in the transition region becomes unstable. In particular, this lowest-order theory predicts that below $\eta = \eta_\star \equiv 12\pi^4 L_y/(3+\pi^2)$ the system is governed by the symmetric branch, whereas above $\eta_\star$ the system is governed by the asymmetric branch. However, higher-order corrections to the small-amplitude approximation allow for the stabilization of the third branch in the region $\eta_- < \eta < \eta_+$, where η_- and η_+ converge to $\eta_\star$ as Δ diminishes to zero.

This behavior is demonstrated in Fig. 2(a), which presents the state diagram of the quasistatic solution on the $(\eta L_x/\eta_\star, \Delta)$ plane. Note that our definition of η differs slightly from that in Ref. [10] and leads to the multiplication of the values on the x axis by L_x. Since $L_x = 1 - \Delta$, this correction is negligible in the small-amplitude approximation, but it affects the theory at higher orders. The diagram consists of three regions that correspond to the symmetric, asymmetric, and intermediate regions. The stability of the intermediate region shrinks to zero at $\eta_\star$ when Δ diminishes. A numerical example of the evolution of the system along a line of constant Δ is presented in Figs. 2(b) and 2(c).

With this quasistatic analysis in mind, our objective is to determine the minimum frequency of vibrations that is associated with each of these solutions.

III. THE SMALL-AMPLITUDE APPROXIMATION AND THE MODAL EXPANSION

In this section, we simplify the general formulation to the small-amplitude approximation ($\Delta \ll 1$) and introduce the modal expansion of the elastic and hydrodynamic fields.

If the amplitude of the sheet is assumed to be small compared with its total length, we can approximate the geometric constraints, Eq. (4), by $\partial y_{\rm sh}/\partial s \simeq \theta$ and $\partial x_{\rm sh}/\partial s \simeq 1 - \frac{1}{2}(\partial y_{\rm sh}/\partial s)^2$. With these approximations, the lateral displacement, Eq. (7a), is given by

$$\frac{1}{2}\int_0^1 \left(\frac{\partial y_{\rm sh}}{\partial x}\right)^2 dx = \Delta, \tag{9}$$

where we replace the coordinate s with the Eulerian coordinate x, according to our level of approximation. Note that in our problem the wavelength of the sheet scales with its total length L. As a result, Eq. (9) implies that the amplitude of the sheet scales as $y_{\rm sh}(s,t) \sim \sqrt{\Delta}$. This scaling is used later to approximate the hydrodynamic equations. In addition, in this approximation, the force balance equations, Eqs. (6), are reduced to

$$\frac{\partial^2 y_{\rm sh}}{\partial t^2} + \frac{\partial^4 y_{\rm sh}}{\partial x^4} + F_x(t)\frac{\partial^2 y_{\rm sh}}{\partial x^2} + p_{\rm u}(x,0,t) - p_{\rm d}(x,0,t) = 0, \tag{10}$$

where to leading order the reaction force $F_x(t)$ is solely a function of time.

Equations (9) and (10) approximate only the elastic part of the model. To reduce the fluid's equations, we recall that the density of the fluid is given by $\rho_i(x,y,t) = \rho_i(x,y,0) + \bar{\rho}_i(x,y,t)$, where $\rho_i(x,y,0) = P_i/\eta$ is the homogeneous density in the static equilibrium state, and $\bar{\rho}_i(x,y,t)$ is a small deviation from this equilibrium state. Under static conditions, we expect the normalized density of the fluid to equal one, up to a small correction that emanates from the sheet's configuration, i.e., $\rho_i(x,y,0) \simeq 1 + O(\sqrt{\Delta})$. Correspondingly, we neglect terms of order $\sqrt{\Delta}\phi$ and omit the nonlinear term in Eq. (1c), as applied in the acoustic approximation. For Bernoulli's equation, this

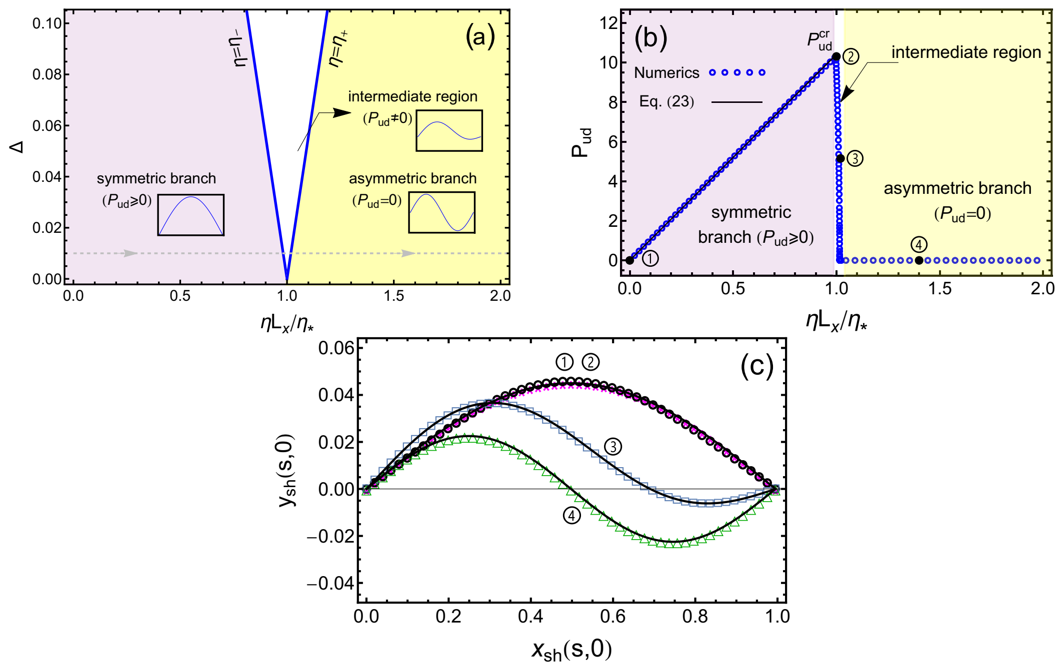

FIG. 2. An overview of the quasistatic solution. (a) The state diagram of the system on the $(\eta L_x/\eta_\star, \Delta)$ plane. When $\eta < \eta_-$, the system exhibits the symmetric branch (light purple region), where the bending energy dominates over the energy of the fluid. In the opposite scenario, when $\eta > \eta_+$, the system exhibits the asymmetric branch (light yellow region). The intermediate region is confined between $\eta_- < \eta < \eta_+$. Its region of stability approaches zero as Δ diminishes. The evolution of the system along the dashed line ($\Delta = 0.005$) is shown in panels (b) and (c). In panel (b), the pressure difference is plotted as a function of $\eta L_x/\eta_\star$. The numerical data are obtained from the minimization of Eq. (8) with $L_y = 1$. Within the symmetric branch, the pressure difference shows an almost linear rise until it reaches $P_{\rm ud}^{\rm cr} \simeq 3\pi^4\sqrt{\Delta}/2$ at point ②. Subsequently, within the transition region, the pressure difference decreases rapidly but continuously until it diminishes to zero. This marks the system's transition to the asymmetric branch. Within the asymmetric branch, the pressure difference remains zero across all values of η. (c) The sheet's configurations along the trajectory are depicted in panel (b); see the corresponding labeled numbers. In the symmetric branch, points ① and ②, the sheet is close in shape to the first mode of buckling. Across the transition region, the sheet's configuration changes continuously from the first to the second mode of buckling; see, for example, point ③. In the asymmetric branch, the sheet's configuration exhibits the second mode of buckling, point ④. The symbols correspond to the numerical minimization of Eq. (8), and the corresponding solid black lines to the two-mode approximation obtained from Eqs. (23) for the symmetric branch, Eq. (31) for the intermediate region ($P_{\rm ud} = P_{\rm ud}^{\rm cr}/2$), and Eq. (27) for the asymmetric branch.

gives $\bar{\rho}_i \simeq -\frac{1}{\lambda\eta}\frac{\partial\phi_i}{\partial t}$. Substituting these approximations into the equation of state and the continuity equation, we find to leading order

$$p_i = P_i - \frac{1}{\lambda}\frac{\partial\phi_i}{\partial t}, \tag{11a}$$

$$\frac{1}{\lambda\eta}\frac{\partial^2\phi_i}{\partial t^2} = \nabla^2\phi_i. \tag{11b}$$

Note that Eq. (11b) describes the propagation of hydrodynamic waves in the fluid. The normalized phase velocity in this equation, $(\lambda\eta)^{1/2}$, represents the ratio between two timescales: the timescale of the gas, $(L^2/RT)^{1/2}$, which dictates the propagation of disturbances in the flow, and the inertial timescale of the sheet, $L^2(\rho_{\rm sh}h/B)^{1/2}$, which governs the propagation of flexural (out-of-plane) waves. In addition, $P_i = \eta\rho_i(x, y, 0)$, which appears in Eq. (11a), corresponds to the static pressure. We can relate this pressure to the configuration of the sheet by using $\rho_i(x, y, 0) = 1/V_i(0)$, where $V_i(0) = 1 \pm \frac{2}{L_x L_y}\int_0^1 y_{\rm sh}(x, 0)dx$ represents the normalized volumes below (+) and above (−) the sheet. Therefore, in the small-amplitude approximation, the static pressure difference in the chamber, $P_{\rm ud} = P_{\rm u} - P_{\rm d}$, is given by

$$P_{\rm ud} = \frac{4\eta}{L_y}\int_0^1 y_{\rm sh}(x, 0)dx. \tag{12}$$

Finally, to close the system of equations in this reduced model, we approximate the kinematic boundary conditions at the sheet-fluid interfaces, Eq. (5), and the hinged conditions of the sheet, Eq. (7c), by

$$\frac{\partial y_{\rm sh}}{\partial t} = \left(\frac{\partial \phi_i}{\partial y}\right)_{y=0}, \tag{13a}$$

$$\frac{\partial^2 y_{\rm sh}}{\partial x^2}(0, t) = \frac{\partial^2 y_{\rm sh}}{\partial x^2}(1, t) = 0. \tag{13b}$$

Equations (9)–(13), supplemented by the boundary conditions at the fluid-chamber interface, Eq. (3), and the end conditions of the sheet, Eq. (7b), form a closure and describe the system's evolution in the limit $\Delta \ll 1$. However, before delving into the linear stability analysis of these equations, we perform two additional steps. First, we express the system of equations by using a variational approach. In Appendix C, we show that the equations and the boundary conditions within the small-amplitude approximation are derived from minimization of the action $\mathcal{S} = \int_0^{\mathcal{T}} \mathcal{L}dt$, where $\mathcal{T}$ is the duration of the experiment and the Lagrangian is given by

$$\begin{aligned}\mathcal{L} = &\int_0^1 \left[\frac{1}{2}\left(\frac{\partial y_{\rm sh}}{\partial t}\right)^2 - \frac{1}{2}\left(\frac{\partial^2 y_{\rm sh}}{\partial x^2}\right)^2 + F_x(t)\left(\frac{1}{2}\left(\frac{\partial y_{\rm sh}}{\partial x}\right)^2 - \Delta\right)\right.\\ &\left. + \frac{1}{\lambda}[\phi_{\rm d}(x, 0, t) - \phi_{\rm u}(x, 0, t) + \lambda t P_{\rm ud}]\frac{\partial y_{\rm sh}}{\partial t}\right]dx\\ &+ \frac{1}{2\lambda}\int_0^{\frac{L_y}{2}}\int_0^1 \left[\frac{1}{\eta\lambda}\left(\frac{\partial \phi_{\rm u}}{\partial t}\right)^2 - |\nabla\phi_{\rm u}|^2\right]dxdy + \frac{1}{2\lambda}\int_{-\frac{L_y}{2}}^0\int_0^1 \left[\frac{1}{\eta\lambda}\left(\frac{\partial \phi_{\rm d}}{\partial t}\right)^2 - |\nabla\phi_{\rm d}|^2\right]dxdy.\end{aligned} \tag{14}$$

The first two terms in the first line of Eq. (14) represent the kinetic and potential energies of the sheet. The third term in this line addresses the constraint related to the sheet's excess length [Eq. (9)], with $F_x(t)$ being a Lagrange multiplier. The term in the second line accounts for the interaction between the sheet and the fluid. Upon minimization, this term contributes to the kinematic boundary conditions [Eq. (13a)] and the hydrodynamic pressures in the force balance equation [Eq. (10)]. The terms in the third line of Eq. (14) pertain to the dynamics of the fluid.

The second step that we take to simplify the model involves a modal expansion, which is further discussed in the following section.

A. Modal expansion

The boundary conditions at the fluid-chamber interfaces are all satisfied if the following Fourier expansions are considered for the potential functions

$$\phi_i(x, y, t) = \sum_{m=0}^{\infty} a_m^i(t)\cos(\pi m x)\cos\left[q_m\left(y \pm \frac{L_y}{2}\right)\right], \tag{15}$$

where the $\pm$ signs correspond, respectively, to the lower (plus) and the upper (minus) parts of the chamber, and q_m and $a_m^i(t)$ are as yet unknown constants and time-dependent functions, respectively. Note that if $\partial y_{\rm sh}/\partial t \neq 0$, as expected in this analysis, the kinematic boundary conditions (13a) imply that $a_m^{\rm d}(t) = -a_m^{\rm u}(t)$. Therefore, hereafter we eliminate $a_m^{\rm u}(t)$ in favor of $a_m^{\rm d}(t)$.

Note also that, in the y direction, the wave numbers are initially unknown, because they depend on the configuration of the sheet. In general, q_m can take either real or imaginary values. While a real wave number corresponds to an oscillating wave pattern, an imaginary q_m corresponds to a wave that is localized around the area of the sheet. In addition, in contrast to the case of an incompressible fluid, the wave numbers q_m typically differ from their counterparts in the x direction. For incompressible fluids, the wave numbers in the x and y directions are always equal, because the continuity equation [Eq. (11b)] reduces to Laplace's equation [12,22,23].

Just as with the potential functions, the following Fourier expansion of the sheet's height function satisfies the hinged boundary conditions:

$$y_{\rm sh}(x,t) = \sum_{n=1}^{\infty} A_n(t)\sin(\pi n x), \tag{16}$$

where $A_n(t)$ are unknown functions that are yet to be determined. Equations (15) and (16) include a summation over infinite terms. In practice, however, we limit these summations to a finite number of modes. It can be shown that if Eq. (16) is truncated after N modes, then the summation in Eq. (15) should be truncated at $N-1$, so as to obtain a closed system of equations for the unknown coefficients.

The Fourier expansions, Eqs. (15) and (16), exhibit the dependence of the potential functions and the height functions on the spatial coordinates. As such, we can substitute these expansions in the Lagrangian, Eq. (14), and integrate over the spatial coordinates. This integration gives

$$\begin{aligned}\mathcal{L} &= \sum_{n=1}^{N}\left[\frac{1}{4}\left(\frac{dA_n}{dt}\right)^2 - \frac{\pi^2 n^2}{4}(\pi^2 n^2 - F_x(t))A_n^2 + tP_{\rm ud}W_1(n,0)\frac{dA_n}{dt}\right] - F_x(t)\Delta \\ &+ \frac{2}{\lambda}\sum_{n=1}^{N}\sum_{m=0}^{N-1} W_1(n,m)\cos\left(\frac{q_m L_y}{2}\right)a_m^{\rm d}(t)\frac{dA_n}{dt} \\ &+ \frac{1}{2\lambda}\sum_{m=0}^{N-1}\left[\frac{1}{\eta\lambda}W_2(q_m)\left(\frac{da_m^{\rm d}}{dt}\right)^2 - \left[\pi^2 m^2 W_2(q_m) + q_m^2 W_3(q_m)\right]\left(a_m^{\rm d}\right)^2\right],\end{aligned} \tag{17}$$

where $P_{\rm ud}$ is the pressure difference in the static state, $W_1(n,m) = \frac{n}{\pi}\frac{1-(-1)^{n+m}}{n^2-m^2}$ for $n \neq m$ and zero otherwise, and

$$W_j(q_m) = (1+\delta_{m0})\left(\frac{L_y}{4} \pm \frac{\sin(q_m L_y)}{4q_m}\right), \tag{18}$$

where the $\pm$ signs correspond, respectively, to $j = 2$ (plus) and $j = 3$ (minus), and δ_{mn} is the Kronecker delta.

Equation (17) signifies a significant simplification of our model. Rather than having to solve a complex system of coupled partial differential equations, we now need to find the modal amplitudes $A_n(t)$ and $a_m(t)$, the wave numbers q_m, and the lateral compression $F_x(t)$. This direction is particularly simple and enables some analytical progress when only a few modes dominate the motion, as we now show happens in this system.

IV. LINEAR STABILITY

To perform the linear stability analysis, we first perturb the modal amplitudes and the lateral compression force around their base solutions, i.e., $A_n(t) = A_n(0) + \epsilon e^{i\omega t}\bar{A}_n$ and

$F_x(t) = F_x(0) + \epsilon e^{i\omega t}\bar{F}_x$, where $A_n(0)$ and $F_x(0)$ are the base solutions, ω is the frequency of the vibrations, which is as yet unknown, $\bar{A}_n$ and $\bar{F}_x$ are unknown constants, and $\epsilon \ll 1$ is the small expansion coefficient. Additionally, since the fluid is at rest in the static configuration, the expansion of the hydrodynamic potential is expressed as $a_m^{\mathrm{d}}(t) = \epsilon e^{i\omega t}\bar{a}_m^{\mathrm{d}}$, where $\bar{a}_m^{\mathrm{d}}$ are unknown constants. Second, we minimize the Lagrangian, Eq. (17), with respect to the coefficients $A_n(t)$ and $a_m^{\mathrm{d}}(t)$, and the lateral compression $F_x(t)$, and then expand the resulting equations in powers of ϵ.

To leading order, order ϵ^0, we obtain

$$n = 1, 2, \ldots, N: \quad \pi^2 n^2[\pi^2 n^2 - F_x(0)]A_n(0) = -2P_{\mathrm{ud}}W_1(n, 0), \tag{19a}$$

$$\sum_{n=1}^{N} \frac{\pi^2 n^2}{4} A_n(0)^2 = \Delta, \tag{19b}$$

where the static pressure difference P_{ud} is given by Eq. (12). In the modal expansion, this equation reads

$$P_{\mathrm{ud}} = \frac{4\eta}{L_y}\sum_{k=1}^{N} W_1(k, 0)A_k(0). \tag{20}$$

Given the lateral displacement Δ, the parameter η, and the vertical dimension L_y, we can solve Eqs. (19) and (20) to obtain the quasistatic state of the system.

In the next order, order ϵ, the equations for the perturbed fields read

$n = 1, 2, \ldots, N:$

$$[-\omega^2 + \pi^4 n^4 - \pi^2 n^2 F_x(0)]\bar{A}_n - \pi^2 n^2 A_n(0)\bar{F}_x = -\frac{4i\omega}{\lambda}\sum_{m=0}^{N-1}\cos\left(\frac{q_m L_y}{2}\right)W_1(n, m)\bar{a}_m^{\mathrm{d}}, \tag{21a}$$

$m = 0, 1, \ldots, N-1:$

$$\left[\left(-\frac{\omega^2}{\lambda\eta} + \pi^2 m^2\right)W_2(q_m) + q_m^2 W_3(q_m)\right]\bar{a}_m^{\mathrm{d}} = 2i\omega\sum_{n=1}^{N}\cos\left(\frac{q_m L_y}{2}\right)W_1(n, m)\bar{A}_n, \tag{21b}$$

$$\sum_{n=1}^{N} n^2 A_n(0)\bar{A}_n = 0. \tag{21c}$$

Equations (21) form a homogeneous system of $2N+1$ equations for the unknown perturbations $\bar{A}_n$, $\bar{a}_m^{\mathrm{d}}$, and $\bar{F}_x$. These equations always have the trivial solution, where all the perturbations are identically zero, unless their corresponding determinant vanishes. However, in our problem, this vanishing determinant condition depends not only on the frequency ω, as is usually encountered in an eigenvalue problem, but also on the wave numbers q_m. In the following analysis, we approximate these wave numbers such that the wave equations, Eq. (11b), are satisfied for each of the Fourier modes in the potential functions (15), i.e.,

$$q_m = \sqrt{\frac{\omega^2}{\lambda\eta} - \pi^2 m^2}. \tag{22}$$

We now add two remarks regarding this selection of wave numbers. First, if, for any value of m, $\omega/\sqrt{\lambda\eta} < \pi m$, then the term under the square root becomes negative, and the wave associated with that specific m in the expansion of the potential functions, Eq. (15), is localized in the y direction. Since we normalized all lengths by L, the decay length of each of these localized waves scales with the total length of the sheet. Conversely, if $\omega/\sqrt{\lambda\eta} > \pi m$ for a particular value of m, the wave in the y direction is not localized but oscillates in the y direction. Second, with this selection of the fluid's wave numbers, the eigenvalue problem has a somewhat unusual form of $\mathbf{A}(\omega)\mathbf{u} = \omega^2\mathbf{u}$, where $\mathbf{u} = \{\bar{A}_1, \ldots, \bar{A}_N, \bar{a}_0^{\mathrm{d}}, \ldots, \bar{a}_{N-1}^{\mathrm{d}}, \bar{F}_x\}$, and $\mathbf{A}(\omega)$ is a matrix that depends on the eigenvalue ω.

In summary, to obtain the lowest eigenmode of the system around a prebuckled state, we first solve Eqs. (19) and (20) for the static equilibrium state. Then, we substitute this solution into Eqs. (21), where q_m is given by Eq. (22), and solve an eigenvalue problem for the lowest frequency ω and the unknown perturbation constants $\bar{A}_n$, $\bar{a}_m^{\mathrm{d}}$, and $\bar{F}_x$. In the subsequent sections, we derive the lowest eigenmode around the base states that correspond to the symmetric and asymmetric branches. We remind the reader that the solution in the transition region is not properly captured by the small-amplitude approximation, and therefore that region is treated in less depth by using our numerical approach.

A. Symmetric branch

In the symmetric branch, the sheet's height function is symmetric around the chamber's midaxis, $x = 1/2$, and the base solution is comprised only of the odd modes, i.e., $A_n(0) = 0$, when $n = 2, 4, 6, \ldots$. A reasonable analytical approximation to this solution is obtained when only two modes are considered in the expansion ($N = 2$). In this case, Eqs. (19) and (20) yield $A_2(0) = 0$ and

$$A_1(0) = \frac{2\sqrt{\Delta}}{\pi}, \quad F_x(0) = \pi^2 + \frac{32\eta}{\pi^4 L_y}, \quad P_{\mathrm{ud}} = \frac{16\eta\sqrt{\Delta}}{\pi^2 L_y}. \tag{23}$$

This two-mode solution is plotted in Figs. 2(b) and 2(c), alongside the numerical solution of the quasistatic state. It is shown to align well with the static pressure difference and the height function derived from the minimization of the nonlinear energy, Eq. (8). Note that, as the parameter η approaches zero (low energy gas), the pressure difference in the chamber vanishes, and the solution converges to that expected from a uniaxially compressed sheet without a surrounding gas.

We now exploit this leading-order solution to investigate the modes of vibration by substituting Eq. (23) into the subleading order, Eqs. (21). From Eq. (21c) it becomes apparent that $\bar{A}_1$ is equal to zero. Therefore, while the base solution of the sheet is symmetric, the perturbation is driven primarily by the asymmetric mode. In addition, Eqs. (21a) and (21b) imply that $\bar{F}_x = 0$, and a nontrivial solution, where the ratio $\bar{A}_2/\bar{a}_1^{\mathrm{d}}$ remains arbitrary, is obtained when the following equation is satisfied [24]:

$$\left(\omega^2 - 12\pi^4 + \frac{128\eta}{\pi^2 L_y}\right)\sin\left(\frac{q_1 L_y}{2}\right) = \frac{128\omega^2}{9\pi^2\lambda q_1}\cos\left(\frac{q_1 L_y}{2}\right), \tag{24}$$

where $q_1 = \sqrt{\frac{\omega^2}{\lambda\eta} - \pi^2}$. Equation (24) is a transcendental equation from which we can infer the eigenvalue ω.

As a first step in analyzing the solutions of Eq. (24), we solve the equation for the lowest frequency of vibrations and compare the solution with the linear stability analysis of Eqs. (1)–(7). The comparison is illustrated in Fig. 3(a), where the excess length and the vertical dimension are set at $\Delta = 0.005$ and $L_y = 1$ and various values of the sheet-to-fluid mass ratio λ are considered. Remarkably, the two-mode approximation aligns very closely with the solution obtained from the more general theoretical framework. Consequently, Eq. (24) significantly simplifies our model in the sense that instead of tackling a complex system of equations it allows us to determine the lowest frequency of vibration through the numerical solution of a simple transcendental equation. This simplification enables us to gain valuable insights into the underlying physical behavior of the system, as discussed in the rest of this section.

First, it is interesting to note that the frequency in the two-mode approximation remains independent of the lateral displacement Δ. This independence is consistent with the solution of the more general model, as depicted in Fig. 3(b). Here, the maximum frequency is presented as a function of λ for various values of Δ.

Second, we recall, from the quasistatic analysis (Sec. II A), that the symmetric branch remains stable only up to $\eta_\star = 12\pi^4 L_y/(3 + \pi^2)$, beyond which it is preempted by the asymmetric branch. In the dynamic analysis, this marginal stability state corresponds to $\omega = 0$. By substitution of this

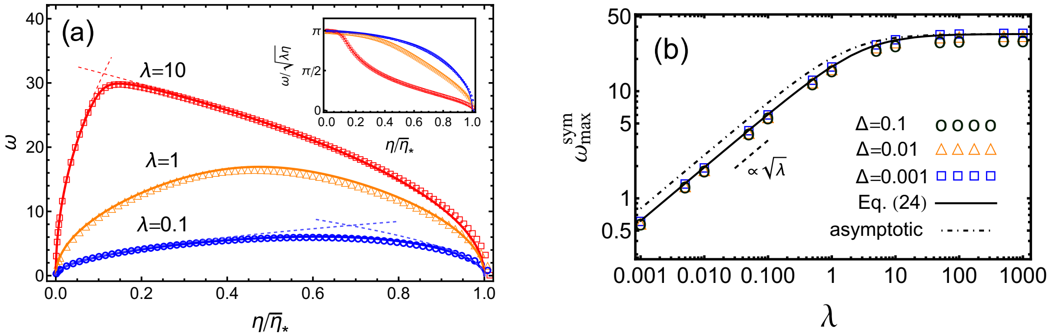

FIG. 3. (a) The frequency ω in the symmetric branch as a function of the parameter $\eta/\bar{\eta}_\star$ for several values of the sheet-to-fluid mass ratio λ. Symbols correspond to the linear stability analysis of Eqs. (1)–(7), and the solid lines with corresponding colors represent the solution of Eq. (24). The dashed lines represent the approximated solutions derived in the limits $\eta/\bar{\eta}_\star \ll 1$ and $0 < 1 - \eta/\bar{\eta}_\star \ll 1$; see Eq. (25). In the inset, $\omega/\sqrt{\lambda\eta}$ is plotted as a function of $\eta/\bar{\eta}_\star$. Since $\omega/\sqrt{\lambda\eta} < \pi$, the wave number in the y direction, q_1, is imaginary, and the flow is localized around the area of the sheet. (b) The maximum frequency in the symmetric branch as a function of λ. Symbols correspond to the linear stability analysis of Eqs. (1)–(7) with different values of Δ, and the solid line represents the solution of the two-mode approximation. The dash-dotted line represents the intersection between the two asymptotic solutions in Eq. (25).

condition into Eq. (24), we find that the symmetric branch is stable only up to $\bar{\eta}_\star = 3\pi^6 L_y/32$. While this marginal stability parameter is very close to $\eta_\star$, it does not coincide with it, i.e., $\eta_\star/\bar{\eta}_\star \simeq 1.007$. This is because we also impose the two-mode approximation on top of the small-amplitude approximation assumed in the quasistatic solution.

However, the solution that we obtain implies that the lowest frequency approaches zero not only when $\eta/\bar{\eta}_\star \to 1$, as expected from the static solution, but also when $\eta/\bar{\eta}_\star \ll 1$. Therefore, in contrast to the quasistatic scenario, where the configuration converges to that expected from a sheet without a surrounding gas, in the dynamic analysis, the frequency of oscillations does not align with the expected frequency of a freely vibrating sheet, which is finite [12]. This finding can be explained as follows: The parameter $(\lambda\eta)^{1/2}$ expresses the normalized phase velocity of waves in the fluid [see Eq. (11b)]. As this parameter approaches zero, the fluid requires more time to complete a cycle of the motion. Because the sheet's motion is synchronized with the fluid, it, too, slows down to match the pace of the fluid. Consequently, this leads to a reduction in the frequency of the vibrations. Here, we emphasize that when taking the limit $\eta/\eta_\star \ll 1$, it is crucial to note that $\Delta \ll \eta/\eta_\star$ since this analysis relies on the small-amplitude approximation. In fact, the system exhibits qualitatively different behaviors near the two asymptotic regions where ω approaches zero. We now examine the solution more closely in these two regions.

1. Asymptotic analysis of the lowest frequency

When η approaches zero, or when η approaches $\bar{\eta}_\star$, Eq. (24) yields, to leading order, the following asymptotic solutions:

$$\eta/\bar{\eta}_\star \ll 1: \ \omega \simeq \pi\sqrt{\lambda\eta}, \tag{25a}$$

$$0 < 1 - \eta/\bar{\eta}_\star \ll 1: \ \omega \simeq \omega_{\rm in}^{\rm sym}\sqrt{\frac{\bar{\eta}_\star - \eta}{\bar{\eta}_\star}}, \quad \omega_{\rm in}^{\rm sym} \equiv \frac{2\sqrt{3}\pi^2}{\sqrt{1 + \frac{128\coth(\pi L_y/2)}{9\pi^3\lambda}}}. \tag{25b}$$

These approximations are plotted in Fig. 3(a) for the cases where $\lambda = 10$ and $\lambda = 0.1$ (dashed lines). When the sheet is much heavier than the fluid (large λ), Eq. (25b) offers a very accurate approximation across the entire range of $\eta/\bar{\eta}_\star$, except for a small region near $\eta/\bar{\eta}_\star$ where the frequency rapidly approaches zero. In contrast, when the sheet is relatively lighter than the fluid (small λ), the validity of Eq. (25a) spans a much wider region of $\eta/\bar{\eta}_\star$, while the region of validity of Eq. (25b) shrinks to the vicinity of $\bar{\eta}_\star$.

The transition between the two regions occurs approximately when ω is maximized. Therefore, we can further quantify the transition by equating Eqs. (25b) and (25a). This gives

$$\eta_{\mathrm{peak}}/\bar{\eta}_\star \simeq \frac{1152}{1152 + 9\pi^4\lambda + 128\pi \coth(\pi L_y/2)}, \tag{26a}$$

$$\omega_{\max}^{\mathrm{sym}} \simeq \frac{2\sqrt{3}\pi^2}{\sqrt{1 + \frac{128\coth(\pi L_y/2)}{9\pi^3\lambda} + \frac{1152}{9\pi^4\lambda Ly}}}, \tag{26b}$$

where η_{peak} approximates the value of η in the maximum frequency, $\omega(\eta_{\mathrm{peak}}) \simeq \omega_{\max}^{\mathrm{sym}}$. Equation (26b) is plotted in Fig. 3(b) for a comparison with the numerical data. When $\lambda \gg 1$, the maximum frequency is obtained at $\eta_{\mathrm{peak}}/\bar{\eta}_\star \simeq 128/(\pi^4 L_y \lambda)$, which gives $\omega_{\max}^{\mathrm{sym}} \simeq 2\sqrt{3}\pi^2$ for the maximum frequency. Consequently, the rapid decrease in the frequency is confined to the region $\eta \in [0, \eta_{\mathrm{peak}}]$, whose width shrinks to zero as $1/\lambda$. In contrast, when $\lambda \ll 1$, we find that $\eta_{\mathrm{peak}}/\bar{\eta}_\star \simeq 9/[9 + \pi L_y \coth(\pi L_y/2)]$ converges to a constant that is independent of λ. The maximum frequency in this region diminishes to zero as $\omega_{\max}^{\mathrm{sym}} \propto \lambda^{1/2}$, as shown in Fig. 3(b).

These scalings for the maximum frequencies characterize the more general solution near $\bar{\eta}_\star$ ($\eta \gtrsim \eta_{\mathrm{peak}}$). This finding may be explained as follows: when $\lambda \gg 1$, the sheet is much heavier than the fluid, and the hydrodynamic effect on the sheet's motion becomes negligible. As a result, the elastic forces of bending and lateral compression are balanced solely by the inertia of the sheet, such that the solution remains independent of the parameter λ. In contrast, when $\lambda \ll 1$, i.e., the sheet is relatively lighter than the fluid, the elastic forces are balanced by the inertia of the fluid, which gives rise to the $\sqrt{\lambda}$ scaling.

However, when $\eta/\bar{\eta}_\star \ll 1$ (or $\eta < \eta_{\mathrm{peak}}$), the solution behaves very differently. In this region, the frequency always scales as $\sqrt{\lambda}$, regardless of the relative densities of the sheet and the fluid. In fact, when the dimensions are retrieved back into the model, we find that the frequency scales as $\sqrt{RT/L^2}$, i.e., neither the inertia of the sheet or of the fluid (ρ_{sh} and ρ_{g}) nor the bending modulus affects the frequency. This suggests that the waves in the chamber become insensitive to the characteristics of the sheet and behave as if the chamber's walls are all rigid. Indeed, in Appendix D, we show that Eq. (25a) coincides with the lowest frequency obtained in a rectangular chamber whose walls are all rigid. To further characterize the solution, we now analyze the eigenfunctions associated with these oscillations.

2. Mode of vibrations

We begin this analysis by observing that, while the base solution of the sheet is symmetric, its corresponding eigenfunction is primarily comprised of asymmetric modes. In the two-mode approximation, the eigenfunction of the sheet is given solely by the second mode $\bar{A}_2$. Indeed, the numerical eigenfunction plotted in Fig. 4(a) confirms this analytical prediction. The motion of the sheet is demonstrated schematically in the inset. When the asymmetric eigenfunction oscillates on top of the symmetric base solution, the sheet appears to move from left to right, while its midpoint remains stationary.

The above oscillations of the sheet induce a vortexlike patterned flow in the chamber that is centered around the stationary point of the sheet [see Fig. 4(b)]. Interestingly, the magnitude of the fluid's velocity decays away from the sheet, suggesting that the wave in the y direction is localized. To verify this notion, we return to Fig. 3(a) and rescale the y axis by $\sqrt{\lambda\eta}$ (see the inset of this figure). Since the wave number in the y direction is determined by $q_1 = \sqrt{\frac{\omega^2}{\lambda\eta} - \pi^2}$, a localized wave corresponds to an imaginary q_1, where $\omega/\sqrt{\lambda\eta} < \pi$. Therefore, the inset in Fig. 3(a) does indeed confirm that the wave is localized in the y direction for all values of η and λ. The localization is maximized when $\eta/\bar{\eta}_\star$ approaches one ($q_1 \to i\pi$); however, when $\eta/\bar{\eta}_\star \ll 1$ the wave number

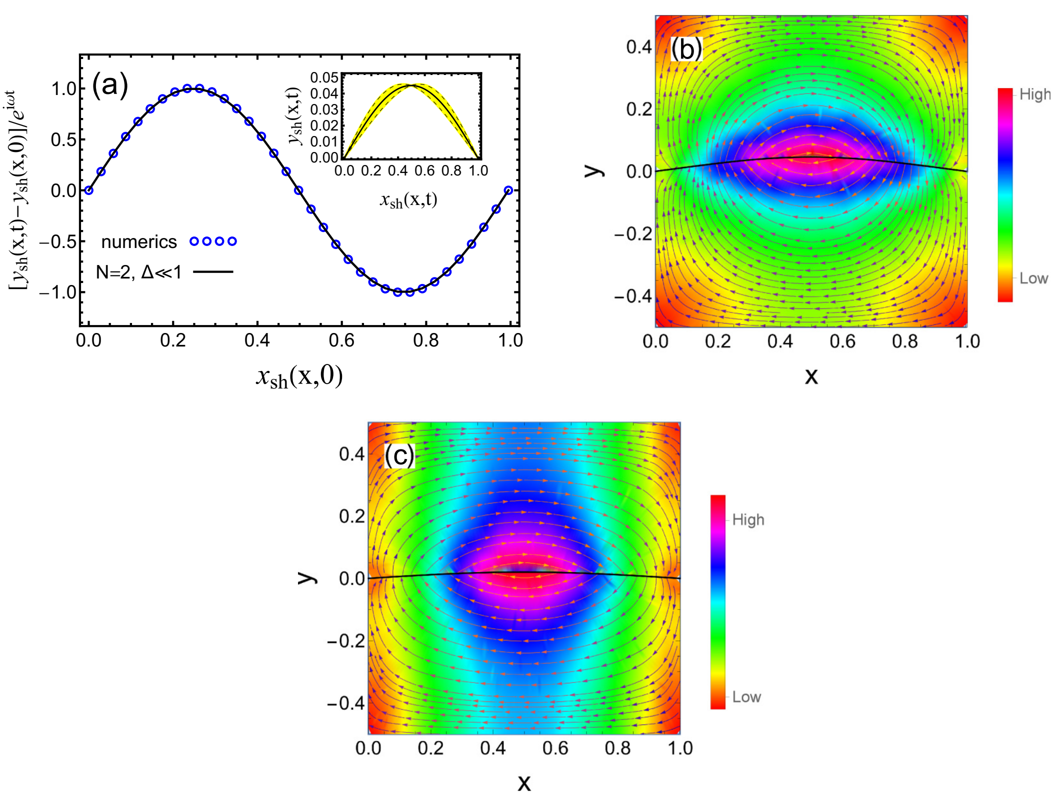

FIG. 4. Eigenfunctions in the symmetric branch. The results in panels (a) and (b) correspond to $\lambda = 10$, $\Delta = 0.005$, and $\eta/\eta_\star = 0.95$. (a) The sheet's eigenfunction is composed primarily of the second mode. Symbols represent the linear stability analysis of Eqs. (1)–(7), while the solid black line represents the eigenfunction derived from the two-mode approximation. The eigenfunctions are normalized such that $[y_{\rm sh}(1/4, t) - y_{\rm sh}(1/4, 0)]/e^{i\omega t} = 1$. (b) The fluid's eigenfunction obtained from the linear stability analysis of the nonlinear model, Eqs. (1)–(7). The eigenfunction displays a localized vortexlike flow around the sheet's midpoint. (c) The fluid's numerical eigenfunction in the case where $\lambda = 10$, $\Delta = 0.001$, and $\eta/\eta_\star = 0.15$. While the eigenfunction still displays a vortexlike flow around the sheet's midpoint, the pattern decays more slowly than that in panel (b).

diminishes to zero ($q_1 \to 0$) and the localized pattern is replaced by an extended wave [compare Figs. 4(b) and 4(c)].

Close to $\bar{\eta}_\star$, where the localization is maximized ($q_1 \to i\pi$), the wave number in the y direction becomes similar to that in the x direction, and the motion of the fluid resembles a mode of vibrations that appears in an incompressible fluid. Therefore, as η approaches $\bar{\eta}_\star$, compressibility effects reduce the frequency only by a factor of $\sqrt{(\bar{\eta}_\star - \eta)/\bar{\eta}_\star}$, which slows down the dynamics, but does not affect the spatial pattern of the flow. Interestingly, in that limit, the coefficient $\omega_{\rm in}^{\rm sym}$ in Eq. (25b) also coincides with the frequency of vibrations of a sheet in an incompressible fluid (see the derivation in Appendix E).

In contrast, when $\eta/\bar{\eta}_\star \ll 1$, the wave number in the y direction approaches zero ($q_1 \to 0$), and the fluid's potential functions become nearly independent of the y coordinate. Consequently, the fluid's velocity is oriented predominantly in the x direction, $\phi_i \sim \cos(\pi x)$, similar to the lowest mode of vibration of a compressible fluid in a chamber with rigid walls (see Appendix D). Therefore, in this limit, the oscillations of the sheet are suppressed in favor of the periodic compression of the gas. We note that if the vertical dimension of the chamber exceeds a certain threshold, this lowest mode solution is preempted by a different solution that corresponds to oscillations of the fluid in the y direction, but we do not delve into these details here (see discussion in Appendix D).

B. Asymmetric branch

The base solution in the asymmetric branch consists of the second mode of buckling, and therefore the solution of Eqs. (19) is given by

$$A_2(0) = \frac{\sqrt{\Delta}}{\pi}, \quad F_x(0) = 4\pi^2, \quad P_{\rm ud} = 0, \tag{27}$$

where $A_n(0) = 0$ for all $n \neq 2$. In Fig. 2(c) (point ④), we plot this approximation of the sheet's configuration and show that it agrees well with the minimization of the nonlinear energy.

In a previous publication [25], it was demonstrated that without a confining fluid this base solution is always unstable, as its corresponding growth rate (imaginary frequency) is always real and positive. However, when the chamber is filled with a fluid, the system tends to stabilize the second mode, since the fluid exerts pressure on the sheet that resists its motion. When this pressure exceeds a critical value, i.e., critical η, the sheet can no longer escape from the second mode, and the system stabilizes.

After this stabilization, the system exhibits two different solutions as a function of η. The first solution is obtained close to the stabilization point, where, on the one hand, the pressures exerted by the fluid on the sheet are large enough to stabilize the sheet, but, on the other hand, the sheet's bending energy is not negligibly small compared with the energy of the fluid. In this case, the sheet induces compressional modes of vibrations, which periodically change the volumes of the chamber. The second solution appears when the energy of the fluid becomes much larger than the bending rigidity of the sheet, i.e., for very large η. In this case, the system behaves as if the fluid were incompressible, where compressional modes are suppressed from the dynamics, but modes of vibrations that induce vortexlike patterned flows are allowed. This is because vortexlike modes allow for the fluid's motion without its compression. These two different solutions are further explored in the subsequent sections.

1. Compressional modes in the asymmetric branch

To obtain the solution in the first region, i.e., close to stabilization, we can apply the two-mode approximation, because compressional modes are driven primarily by the oscillations of the first mode, while the initial configuration of the sheet is determined by the second mode. Indeed, substituting the base solution, Eq. (27), in the subleading order, Eq. (21), we immediately find that $\bar{A}_2 = 0$. In addition, all the equations are satisfied when $\bar{F}_x = 0$, $\bar{A}_1/\bar{a}_0^{\rm d}$ remains arbitrary, and the following equation is satisfied:

$$q_0 \sin(q_0 L_y)(\omega^2 + 3\pi^4) = \frac{32\omega^2}{\pi^2\lambda}\cos^2\left(\frac{q_0 L_y}{2}\right), \tag{28}$$

where $q_0 = \omega/\sqrt{\lambda\eta}$ is the wave number of the flow in the y direction. It can readily be verified that as η approaches zero, the lowest solution of Eq. (28) converges to $\sigma \equiv i\omega = \sqrt{3}\pi^2$, which coincides with the growth rate of a sheet that is unconstrained by a surrounding fluid. This solution implies that the asymmetric branch is unstable and that any small perturbation will drive an exponentially diverging dynamics, in the vicinity of that perturbation. As η deviates from zero, the growth rate σ decreases until it approaches zero at $\eta = \bar{\eta}_\star$. This marks the stabilization of the asymmetric branch, and the starting point of our lowest frequency analysis.

In Fig. 5(a), we compare the lowest solution of Eq. (28) with the results of the linear stability analysis of the more general model, Eqs. (1)–(7). This comparison is carried out for the case where $\Delta = 0.005$ and $L_y = 1$, and for three different values of λ. While there is reasonable agreement between the numerical and analytical data, some visible discrepancies emerge at lower values of

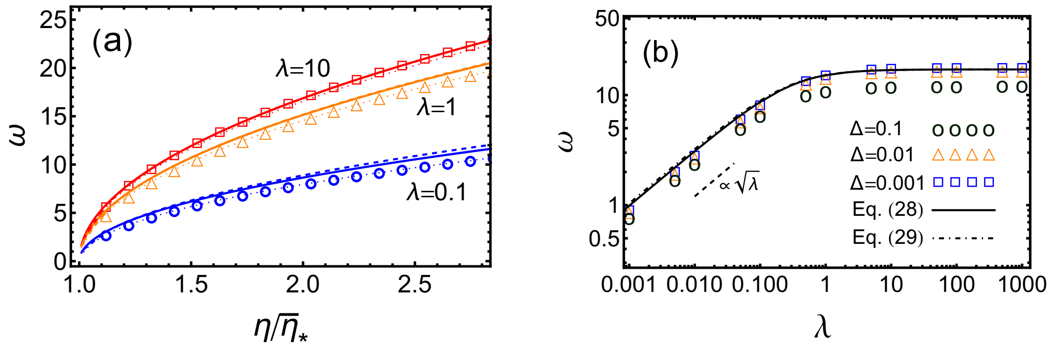

FIG. 5. (a) The frequency ω as a function of $\eta/\bar{\eta}_\star$. Symbols correspond to the linear stability analysis of Eqs. (1)–(7), with all the data points being obtained at $\Delta = 0.005$ and $L_y = 1$. The solid lines with corresponding colors indicate the lowest nonzero solutions of Eq. (28). The dotted lines represent solutions obtained from Eqs. (21) with $N = 3$, and the dashed lines are based on Eq. (29). (b) The frequency ω is plotted as a function of the sheet-to-fluid mass ratio λ, with $\eta = 2\bar{\eta}_\star$ and $L_y = 1$. Symbols correspond to the linear stability analysis of Eqs. (1)–(7) with different values of Δ. The solid and dot-dashed black lines represent the solution of Eq. (28) and the approximated solution given by Eq. (29), respectively.

λ. These discrepancies can be addressed by utilizing a higher number of modes, say $N = 3$, in the solution of Eqs. (21) [see the dotted lines in Fig. 5(a)].

Regardless these minor discrepancies, we consistently observe that the lowest frequency increases monotonically with $\eta/\bar{\eta}_\star$. Indeed, when Eq. (28) is expanded in powers of $(\eta - \bar{\eta}_\star)^{1/2}$ we obtain

$$1 < \frac{\eta}{\eta_\star} \ll 2: \quad \omega \simeq \frac{\sqrt{3}\pi^2}{\sqrt{1 + \frac{8L_y}{3\pi^2\lambda}}} \sqrt{\frac{\eta - \bar{\eta}_\star}{\bar{\eta}_\star}}. \tag{29}$$

This approximation is plotted alongside the numerical data in Fig. 5(a) (see dashed lines). Interestingly, while Eq. (29) should strictly hold only close to $\eta_\star$, it agrees with the more general solution well beyond its strict limits.

At a fixed value of η, Eq. (29) reveals two distinct behaviors with respect to λ. For $\lambda \gg 1$, the frequency converges to a constant, as is to be expected when the sheet is heavier than the fluid. Conversely, for $\lambda \ll 1$, the scaling $\omega \propto \sqrt{\lambda}$ emerges, which is typical of scenarios where the fluid is relatively heavier than the sheet. Figure 5(b) depicts one such example, and shows ω at $\eta = 2\bar{\eta}_\star$ as a function of λ. Importantly, the plot also shows that the small-amplitude solution is independent of the lateral displacement Δ. As Δ approaches zero, the numerical solution converges to the expected two-mode approximation.

The typical eigenfunctions of the sheet and the fluid in this region of the asymmetric branch are plotted in Fig. 6. As predicted by the two-mode approximation, the sheet's eigenfunction is primarily comprised of the first mode, as shown in Fig. 6(a). Yet, we observe some visible discrepancies between the theoretical and the numerical eigenfunctions, which vanish when higher modes are used in the solution of Eq. (21). When this eigenfunction oscillates on top of the asymmetric base solution, it induces an up-and-down motion of the sheet, as seen in the inset of Fig. 6(a). This oscillatory motion momentarily drives a net flow of fluid in the y direction, as illustrated in Fig. 6(b). The wave number in the y direction is governed primarily by $q_0 = \omega/\sqrt{\lambda\eta}$, and, consequently, unlike the flow in the symmetric branch, this wave number is always real and positive, and always leads to an extended wave pattern in the y direction.

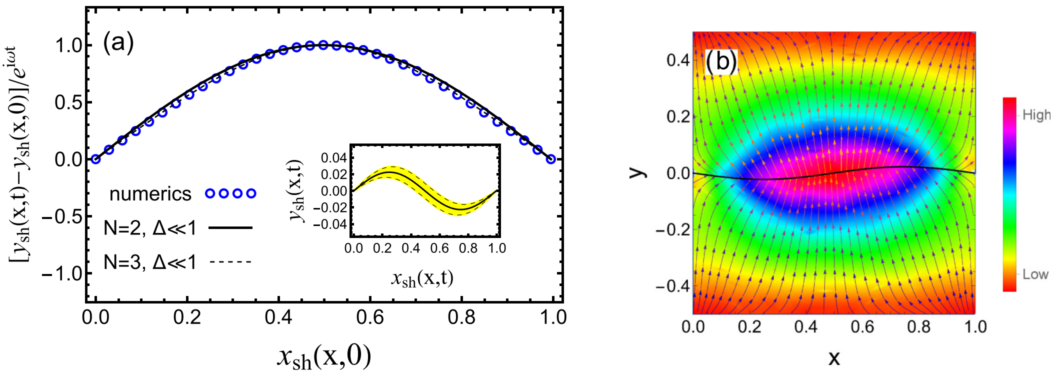

FIG. 6. Eigenfunctions of the sheet and the fluid in the asymmetric branch. In both panels, $\Delta = 0.005$, $L_y = 1$, $\eta = 1.1\eta_\star$, and $\lambda = 10$. (a) The sheet's eigenfunction: Open blue circles represent the results of the linear stability analysis of the nonlinear equations. The black solid line represents the two-mode approximation, and the dashed black line the solution of Eqs. (21) with $N = 3$. Inset: Schematic illustration of the sheet's oscillations. The solid line represents the base solution, and the dashed lines a superposition of the base solution and the perturbation. All eigenfunctions are normalized such that $[y_{sh}(1/2,t) - y_{sh}(1/2,0)]/e^{i\omega t} = 1$. (b) The flow pattern: The sheet's oscillations momentarily induce a net flow in the y direction.

2. *Vortexlike modes in the asymmetric branch*

The solution we obtained immediately above momentarily induces a net change in the volumes of the two parts of the chamber, which leads to the compression of the fluid on the one side and its expansion on the other side of the sheet. However, as the energy of the fluid becomes greater than that of the sheet (i.e., η increases), the net compression of the fluid requires that the sheet exert larger pressures. Therefore, for a fixed bending rigidity, we may expect a limiting value of η beyond which compressional modes of vibration, as depicted in Fig. 6(b), will be suppressed from the dynamics. Indeed, as we increase η in the numerical model beyond the region plotted in Fig. 5(a), we observe that the lowest frequency deviates from the frequency predicted by Eq. (29) and converges to a constant, which is independent of η. After this convergence, the fluid's motion adopts a vortexlike patterned flow rather than the net flow encountered close to $\bar{\eta}_\star$.

To gain further insight into this large-η solution of the asymmetric branch, we note that the two-mode approximation is inadequate to describe this vortexlike mode of vibrations. This limitation arises due to the fact that the two-mode approximation restricts the first mode of the sheet to perturb the second mode, and thereby allows only compressional modes. Indeed, the solution of Eq. (28) increases indefinitely as a function of η and does not resemble convergence to a constant frequency. To analyze this region, we need to go back to Eqs. (19)–(21) and include a higher number of modes in the solution. Fortunately, adding just one additional mode (i.e., $N = 3$) corrects the solution to within a reasonable approximation.

Since the solution of the leading-order equations, Eqs. (27), is valid for any number of modes, we can readily undertake the analysis of the subleading order, Eqs. (21). However, considering the limit $\eta/\bar{\eta}_\star \gg 1$ in these equations is not a straightforward task, and thus we elaborate on some of its details. In this limit, the frequency converges to a constant, and therefore the wave numbers that correspond to $m > 0$ [Eq. (22)] reduce to $q_m = i\pi m$; i.e., the dynamics is governed by localized waves, rather than extended waves. In addition, for $m = 0$, we have that $q_0 \ll 1$, such that $\cos(q_0 L_y/2) \simeq 1$ and $\sin(q_0 L_y) \simeq q_0 L_y$.

Seemingly, with this last reduction, it appears that the zero-order mode of the potential functions, i.e., the term akin to $a_0^{\mathrm{d}}(t)$ in Eq. (15), reduces to a time-dependent constant that has a negligible effect on the fluid's velocity. However, this term may not be neglected in the analysis, because it still affects the hydrodynamic pressure, which, in turn, influences the sheet's motion. More precisely, using the above assumptions, we obtain from Eq. (21b) that $\bar{a}_0^{\mathrm{d}} = \frac{2i\lambda\eta}{\omega L_y}\sum_{n=1}^{N} W_1(n,0)\bar{A}_n$. Thus, when

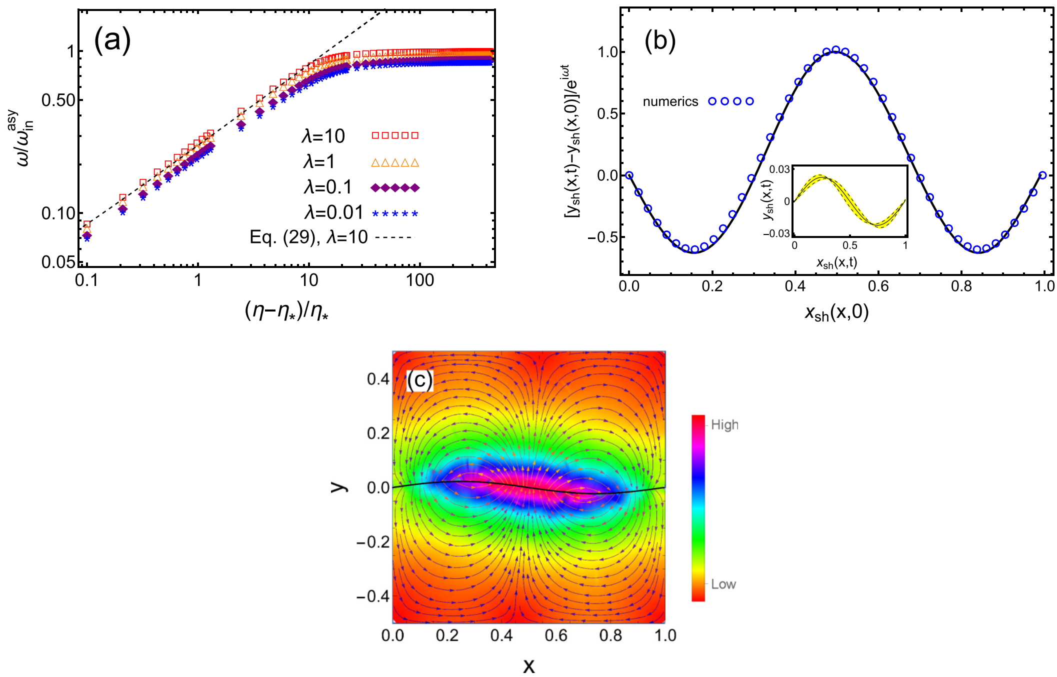

FIG. 7. Lowest frequency and the mode of vibrations in the large-η solution. In all the panels, the symbols correspond to the linear stability analysis of Eqs. (1)–(7), where $\Delta = 0.01$ and $L_y = 1$. (a) The frequency ω, normalized by $\omega_{\text{in}}^{\text{asym}}$, Eq. (30), as a function of $(\eta - \bar{\eta}_\star)/\bar{\eta}_\star$. The numerical data are plotted for several values of the parameter λ. The dashed black line corresponds to Eq. (29) with $\lambda = 10$. Up to η_{tran}, the frequency scales as $\sqrt{(\eta - \bar{\eta}_\star)/\bar{\eta}_\star}$, whereas above η_{tran} it converges to a constant, which is independent of η. (b) The sheet's eigenfunction comprises a superposition of the first and third modes. The solid black line represents the analytic approximation $[y_{\text{sh}}(x, t) - y_{\text{sh}}(x, 0)]/e^{i\omega t} = [\sin(\pi x) - 3\sin(3\pi x)]/4$. The proportions between the amplitudes of the modes is determined so as to keep the volume difference in the chamber equal to zero, i.e., $\sum_{n=1}^{3} W_1(n, 0)\bar{A}_n = 0$. The eigenfunction is normalized such that the perturbation of the sheet's height function equals one at $x = 1/2$. The inset figure shows the vibrations of the sheet schematically, where the solid line represents the base solution, Eq. (27), and the dashed lines represent the superposition of the base solution and the perturbation. (c) The eigenfunction of the fluid's velocity exhibits two counterrotating vortices around $x \simeq 0.3$ and $x \simeq 0.7$, where the eigenfunction of the sheet equals zero.

η increases indefinitely, $\bar{a}_0^{\text{d}}$ diverges and causes the pressure to diverge as well, unless the summation term approaches zero at a rate that scales as $1/\eta$. Physically, this summation accounts for the difference between the upper and the lower volumes of the chamber, $V_{\text{du}}(t) = 2\int_0^1 y_{\text{sh}}(x, t)dx = \epsilon e^{\sigma t}\sum_{n=1}^{N} W_1(n, 0)\bar{A}_n$. Therefore, when η diverges, the system tends to restrict changes in the upper and lower volumes, which, in turn, resemble the limit of an incompressible fluid (see further discussion in Appendix E).

Overall, we find from Eqs. (21) that up to a correction that diminishes to zero as $1/\eta$ the lowest frequency reads

$$N = 3: \quad \omega \equiv \omega_{\text{in}}^{\text{asy}} = \frac{\sqrt{201/5}\pi^2}{\sqrt{1 + \frac{8192\coth(\pi L_y)}{1125\pi^3\lambda}}}, \tag{30}$$

which coincides with that expected in the case of a sheet in an incompressible fluid (see Appendix E). In Fig. 7(a), we plot the lowest frequency, normalized by $\omega_{\text{in}}^{\text{asy}}$, as a function of $(\eta - \bar{\eta}_\star)/\bar{\eta}_\star$. While for relatively small values of η the solution scales as $\sqrt{(\eta - \bar{\eta}_\star)/\bar{\eta}_\star}$, as given by Eq. (29), beyond a certain threshold it converges to a constant, as predicted by Eq. (30). We can estimate the critical η where this transition occurs by equating the two asymptotic solutions, Eqs. (29) and (30). This gives $\eta_{\mathrm{tran}}/\bar{\eta}_\star = 1 + 5025(8\pi L_y + 3\pi^3\lambda)/(1125\pi^3\lambda + 8192\coth(\pi L_y))$, where η_{tran} denotes the critical value of η at the transition from compressional to vortexlike modes. Note that in our numerical analysis $L_y = 1$ and the critical value is almost independent of λ. However, the dependence of η_{tran} on λ becomes more pronounced as L_y increases.

The eigenfunction of the sheet associated with this frequency, which is plotted in Fig. 7(b), exhibits a configuration that comprises a superposition of the first and third modes. The proportions between these modes are determined so as to keep the integral over the sheet's configuration equal to zero, or equivalently, where the volume difference in the chamber equals zero, $\sum_{n=1}^{3} W_1(n,0)\bar{A}_n = 0$. This eigenfunction vanishes to zero at two different points in the bulk of the fluid [26], which, in return, correspond to the centers of two counterrotating vortices [see Fig. 7(c)]. In contrast to the compressional modes, the magnitude of the fluid's velocity in the vortexlike modes decays exponentially in the y direction.

C. Intermediate region

The analysis in the small-amplitude approximation suggests that the sheet's configuration changes discontinuously across $\bar{\eta}_\star$. Indeed, up to $\eta = \bar{\eta}_\star$, the symmetric branch is stable, and the sheet exhibits a configuration that closely resembles the first mode of buckling. However, with a slight increase in η above $\bar{\eta}_\star$, the symmetric branch becomes unstable, the asymmetric branch stabilizes, and the sheet adopts the second mode of buckling. Therefore, it seems that the sheet transitions abruptly from the first to the second mode as η exceeds $\bar{\eta}_\star$. In a previous publication, we demonstrated that this discontinuous transition is, in fact, incorrect and results from our order of approximation. Had we included higher-order corrections of the order of Δ^2, as opposed to Δ, in the elastic energy, we would have observed a continuous transition of the sheet (see the example in Sec. II A). The transition occurs over a narrow region of width Δ and therefore shrinks to zero as Δ diminishes.

This degeneracy of the solution in the intermediate region leaves a signature in the solution of the small-amplitude approximation. Indeed, setting $\eta = \bar{\eta}_\star$ in Eqs. (19) for the base configuration and applying the two-mode approximation yields a new branch of solutions:

$$\eta = \bar{\eta}_\star: \quad A_1(0) = \frac{4P_{\mathrm{ud}}}{3\pi^5}, \quad A_2(0) = \frac{2}{3\pi^5}\sqrt{\left(P_{\mathrm{ud}}^{\mathrm{cr}}\right)^2 - P_{\mathrm{ud}}^2}, \quad F_x(0) = 4\pi^2, \tag{31}$$

where $P_{\mathrm{ud}}^{\mathrm{cr}} = 3\pi^4\sqrt{\Delta}/2$, and the pressure difference P_{ud} remains undetermined but confined to the range $P_{\mathrm{ud}} \in [0, P_{\mathrm{ud}}^{\mathrm{cr}}]$. While the lower bound is set, because we consider only configurations that buckle upwards, the upper bound is set because of the square root dependence in $A_2(0)$. When $P_{\mathrm{ud}} = P_{\mathrm{ud}}^{\mathrm{cr}}$, the modal amplitudes reduce to $A_1(0) = 2\sqrt{\Delta}/\pi$ and $A_2(0) = 0$, and the solution converges to that given by the symmetric branch, Eqs. (23). However, when $P_{\mathrm{ud}} = 0$, we find that $A_1(0) = 0$ and $A_2(0) = \sqrt{\Delta}/\pi$, as given by the asymmetric branch, Eqs. (27). Therefore, Eqs. (31) represent a continuous family of solutions, defined at a single point in the parameter space ($\eta = \bar{\eta}_\star$), which describes a smooth transition of the sheet from the symmetric to the asymmetric configurations. One configuration of this family is plotted in Fig. 2(c) (point ③).

When Eqs. (31) are substituted into the equations at the subleading order, Eqs. (21), the lowest frequency vanishes to zero, and the family of solutions enters a marginal stability state. However, the linear stability analysis of the more general model, Eqs. (1)–(7), reveals a different picture. An example of the evolution of the lowest frequency is presented in Fig. 8(a), where ω is plotted as a function of $\eta L_x/\eta_\star$. Note that here we multiply η by $L_x/\eta_\star$, and not just by $1/\bar{\eta}_\star$, because we focus on a region that is beyond the accuracy of the small-amplitude approximation. This higher-order correction places the intermediate region, for example, symmetrically around one, as depicted in Ref. [10]. Figure 8(a) implies that the symmetric branch is stable only up to η_-, which is slightly smaller than $\eta_\star$, and that the asymmetric branch is stable only down to η_+, which is slightly higher

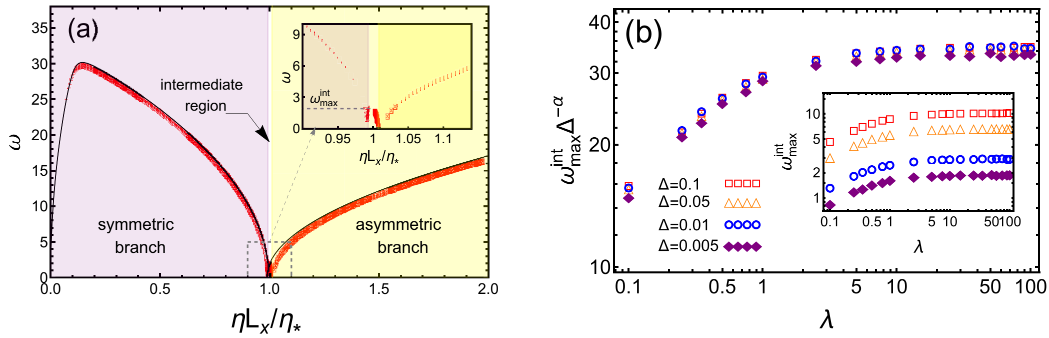

FIG. 8. The lowest frequency in the intermediate region. In both panels, the symbols correspond to the linear stability analysis of Eqs. (1)–(7). (a) The frequency ω as a function of $\eta L_x/\eta_\star$ where $\Delta = 0.005$, $L_y = 1$, and $\lambda = 10$. The plot shows the three different branches of the solutions, where the symmetric branch dominates when $\eta < \eta_-$ (light purple shaded area), the asymmetric branch dominates when $\eta > \eta_+$ (light yellow shaded area), and the intermediate region is stabilized in a narrow region between η_- and η_+ (white background). The solid black lines in the symmetric and asymmetric branches represent the solutions of Eqs. (24) and (28) in the two-mode approximation. The inset presents a magnification of the intermediate region where the frequency increases to a maximum value of $\omega^{\text{int}}_{\text{max}}$ and then decreases to zero. (b) The rescaled maximum frequency $\omega^{\text{int}}_{\text{max}}\Delta^{-\alpha}$ ($\alpha \simeq 0.54$) as a function of λ for several values of the lateral displacement. The data without the scaling are presented in the inset.

than $\eta_\star$. In between η_- and η_+, the intermediate solution is stabilized, and its corresponding lowest frequency is greater than zero. The frequency increases just after the first transition (close to η_-) and then decreases back to zero near the second transition (close to η_+).

The maximum frequency in the intermediate region, $\omega^{\text{int}}_{\text{max}}$ [see the inset in Fig. 8(a)], is plotted in Fig. 8(b) as a function of λ for several values of the lateral displacement Δ. The figure reveals that, in contrast to the symmetric and asymmetric branches, the frequency depends on the lateral displacement even when $\Delta \ll 1$. The numerical data imply that the frequency diminishes to zero

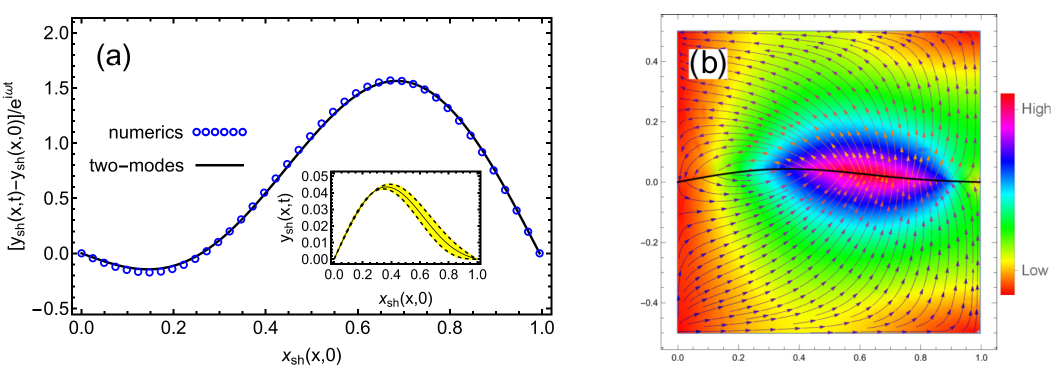

FIG. 9. An example of the eigenfunction in the intermediate region. The data are obtained from the linear stability analysis of Eqs. (1)–(7), where $L_y = 1$, $\lambda = 10$, and $\omega = \omega^{\text{int}}_{\text{max}}$. (a) The eigenfunction of the sheet does not exhibit a specific symmetry but is comprised of a superposition of the first two modes. The solid line is obtained from the first two amplitudes of the Fourier sine spectra of the numerical shape. The inset shows a schematic representation of the sheet's vibration, where the solid line represents the static base solution and the dashed lines represent the compositions of the base solution and the eigenfunction. (b) The flow field obtained from the sheet's vibrations is comprised of a net flow and a vortexlike flow.

approximately as Δ^{α}, where $\alpha \simeq 0.54$. The inset in Fig. 8(b) presents the data before the scaling is applied.

Since the base solution is primarily comprised of the first two modes, as given by Eqs. (31), we anticipate that its corresponding eigenfunction will also be a superposition of these modes. This is because the symmetric contribution to the base solution is perturbed mainly by the odd perturbation $\bar{A}_2$, while the asymmetric contribution is affected primarily by the symmetric perturbation $\bar{A}_1$. An example of the eigenfunction in the intermediate region is plotted in Fig. 9(a) for the case where $\Delta = 0.005$, $\lambda = 10$, and $\omega = \omega_{\max}^{\rm int}$. It is demonstrated that this eigenfunction agrees well with a fitting function that incorporates only the first two modes of the sheet. As the sheet oscillates around the base solution, it induces both a vortexlike flow, due to the contribution of the symmetric perturbation, and a net flow, due to the asymmetric part of the eigenfunction, as can be seen in the example plotted in Fig. 9(b).

V. SUMMARY AND CONCLUSIONS

We studied the interaction between a thin sheet and a compressible fluid medium in a setup comprising a rectangular chamber with a movable piston. The piston compresses a sheet that divides the chamber into two parts. The sheet's compression induces buckling and leads to inhomogeneity between the upper and lower parts of the chamber. Our investigation focused on the system's response to small dynamic excitations by using a linear stability analysis of an elastohydrodynamic model that considers the two-way coupled motion of the sheet and the fluid. While this phenomenon is described by a complex set of equations, which are, in general, intractable, we were able to shed light on some fundamental building blocks that comprise the dynamic self-sustaining pattern formation in the system. For that purpose, we made two assumptions in the analysis of the dynamics: the first was the small-amplitude approximation, and second was a modal expansion of the elastic and hydrodynamic fields. The results of the reduced model fit quite well with the solution of the more general equations.

The linear stability analysis around the symmetric branch produced two interesting results. First, the lowest mode of the system is comprised of a vortexlike patterned flow that is localized around the area of the sheet. The extent of localization scales with the lengths of the sheet and depends strongly on the thermal-to-bending energy ratio. The localization diminishes to zero when $\eta/\bar{\eta}_\star \ll 1$ and approaches a maximum value close to the transition region, $\eta/\bar{\eta}_\star \simeq 1$. Second, the lowest frequency exhibits nonmonotonic behavior as a function of η. The frequency approaches zero in the two asymptotic regions of $\eta/\bar{\eta}_\star \ll 1$ and $\eta/\bar{\eta}_\star \simeq 1$, and, in between those asymptotes, reaches a maximum value that depends on the sheet-to-fluid mass ratio λ.

Slightly beyond $\bar{\eta}_\star$, the symmetric branch becomes unstable, and the asymmetric branch stabilizes. The lowest eigenmode in the asymmetric branch consists of two different solutions. Close to $\bar{\eta}_\star$, the oscillations of the sheet induce periodic compression of the gas. However, far from the transition ($\eta/\bar{\eta}_\star \gg 1$), the thermal energy of the gas becomes much larger than the bending energy of the sheet, and the system, again, exhibits a vortexlike flow centered around the area of the sheet. We showed that the lowest frequency in the latter scenario coincides with that expected in an incompressible fluid. The transition between the symmetric and the asymmetric branches is governed by a third branch of solutions that allows a continuous transition between the first and second modes of the sheet. We showed that the lowest frequency in this region depends strongly on the lateral compression Δ, different from the symmetric and asymmetric solutions, which are almost independent of this parameter.

Early in the formulation, we assumed the fluid to be inviscid and irrotational and imposed isothermal conditions. While meeting all these requirements simultaneously may be challenging in practice, we emphasize that these assumptions were chosen to allow for an analytically tractable framework that captures key aspects of the system's physics. Nonetheless, one may expect that operating such systems would require relatively low frequencies to facilitate temperature equilibration with the environment.

In conclusion, the dynamic interplay between a thin sheet and a compressible fluid medium offers a promising avenue for enhancing the flexibility and efficiency of small-scale devices that requires fine tuning of the lowest mode of vibrations. Harnessing this dynamic interaction not only enhances our understanding of fluid-structure interactions but also paves the way for the development, for example, of more efficient and customizable energy harvesting solutions.

ACKNOWLEDGMENT

This research was partially supported by the Israel Science Foundation (Grant No. 950/22).

APPENDIX A: LINEAR STABILITY ANALYSIS AT A FINITE LATERAL DISPLACEMENT

To derive the linear stability analysis of Eqs. (1)–(7), we first expand the elastic and the hydrodynamic fields around their base solutions. For example, the height function of the sheet is given by $y_{\rm sh}(s,t) = y_{\rm sh}(s,0) + \epsilon e^{i\omega t}\hat{y}_{\rm sh}(s)$, where $y_{\rm sh}(s,0)$ is the quasistatic solution, ω is the unknown frequency, $\hat{y}_{\rm sh}(s)$ is the eigenfunction, and ϵ is an arbitrarily small parameter. Correspondingly, we define the eigenfunctions $\{\hat{x}_{\rm sh}(s), \hat{\theta}(s), \hat{F}_x(s), \hat{F}_y(s)\}$ for the configuration of the sheet, and $\{\hat{\phi}_i(x,y), \hat{p}_i(x,y), \hat{\rho}(x,y)\}$ for the fluid. Note that, in the static state, the fluid is at rest, and therefore $\phi_i(x,y,0) = 0$, $p(x,y,0) = P_i$ and $\rho_i(x,y,0) = P_i/\eta$ are all constants.

Thereafter, we substitute the perturbed fields into Eqs. (1)–(7) and expand them to linear order in ϵ. The equation of state, the continuity equation, and Bernoulli 's equation, Eqs. (1), reduce to

$$\hat{p}_i = \eta\hat{\rho}_i, \tag{A1a}$$

$$i\omega\hat{\rho}_i + \frac{P_i}{\eta}\nabla^2\hat{\phi}_i = 0, \tag{A1b}$$

$$\hat{\rho}_i = -i\frac{\omega P_i}{\lambda\eta^2}\hat{\phi}_i. \tag{A1c}$$

The boundary conditions on the fluid-chamber interfaces are given by

$$\frac{\partial\hat{\phi}_i}{\partial x}(0,y,t) = \frac{\partial\hat{\phi}_i}{\partial x}(1-\Delta,y,t) = 0, \tag{A2a}$$

$$\frac{\partial\hat{\phi}_{\rm u}}{\partial y}(x,L_y/2,t) = \frac{\partial\hat{\phi}_{\rm d}}{\partial y}(x,-L_y/2,t) = 0. \tag{A2b}$$

In addition, the geometric constraints, Eqs. (4), and the force balance equations on the sheet, Eqs. (6), are given to linear order by

$$\frac{d\hat{\mathbf{x}}_{\rm sh}}{ds} = \hat{\theta}\hat{\mathbf{n}}_{\rm d}(s,0), \tag{A3a}$$

$$\frac{d^2\hat{\theta}}{ds^2} = [-F_x(s,0)\hat{\theta} + \hat{F}_y]\cos\theta(s,0) - [\hat{F}_x + \hat{\theta}F_y(s,0)]\sin\theta(s,0), \tag{A3b}$$

$$-\omega^2\hat{\mathbf{x}}_{\rm sh} = -\frac{d\hat{\mathbf{F}}}{ds} + P_{\rm ud}\hat{\theta}\hat{\mathbf{t}}(s,0) - [\hat{p}_{\rm u}(x_{\rm sh},y_{\rm sh}) - \hat{p}_{\rm d}(x_{\rm sh},y_{\rm sh})]\hat{\mathbf{n}}_{\rm d}(s,0), \tag{A3c}$$

where $\hat{\mathbf{t}}(s,0) = (\cos\theta(s,0), \sin\theta(s,0))$ and $\hat{\mathbf{n}}_{\rm d}(s,0) = (-\sin\theta(s,0), \cos\theta(s,0))$ are the tangent and the normal unit vectors, respectively, of the unperturbed configuration. To close the system of equations it remains to expand the kinematic boundary conditions, Eq. (5), and the end support of the sheet, Eqs. (7), to linear order in ϵ. This gives

$$i\omega\hat{\mathbf{n}}_i(s,0)\cdot\hat{\mathbf{x}}_{\rm sh} = \hat{\mathbf{n}}_i(s,0)\cdot\nabla\hat{\phi}_i, \tag{A4a}$$

$$\hat{\mathbf{x}}_{\rm sh}(0) = \hat{\mathbf{x}}_{\rm sh}(1) = 0, \tag{A4b}$$

$$\frac{d\hat{\theta}}{ds}(0) = \frac{d\hat{\theta}}{ds}(1) = 0. \tag{A4c}$$

This completes the derivation of the linear stability analysis of Eqs. (1)–(7). In summary, given the parameters η, Δ, L_y, and λ, we need first to minimize the energy, as given in Eq. (8), and to find the static equilibrium state at $t = 0$. Then, we need to substitute this solution into Eqs. (A1)–(A4). Since these equations are linear and homogeneous, they always yield the trivial solution, where all the perturbation functions equal zero, unless their corresponding determinant vanishes. This condition of the vanishing determinant gives the frequency ω. Once ω is obtained, we can calculate its corresponding eigenfunction.

APPENDIX B: DERIVATION OF THE SYSTEM'S CONSERVED QUANTITY

In this Appendix, we show that Eqs. (1)–(7) have a conserved quantity that corresponds to the total free energy of the system. For that purpose, we first multiply Eq. (6a) by $\partial\theta/\partial t$ and Eq. (6b) by $\partial\mathbf{x}_{\rm sh}/\partial t$. Then, we subtract the second equation from the first and integrate over the configuration of the sheet. This gives

$$\frac{d}{dt}\left[E^{\rm k}_{\rm sh}(t) + E^{\rm p}_{\rm sh}(t)\right] = \int_0^1 \frac{\partial}{\partial s}\left(\frac{\partial\theta}{\partial s}\frac{\partial\theta}{\partial t} - \mathbf{F}\cdot\frac{\partial\mathbf{x}_{\rm sh}}{\partial t}\right)ds - \int_0^1 [p_{\rm u}(x_{\rm sh}, y_{\rm sh}, t) - p_{\rm d}(x_{\rm sh}, y_{\rm sh}, t)]\frac{\partial\mathbf{x}_{\rm sh}}{\partial t}\cdot\hat{\mathbf{n}}ds, \tag{B1}$$

where we use the geometric constraint, Eqs. (4), and integration by parts to simplify the result. In addition, we readily identify the kinetic and the potential energies of the sheet as $E^{\rm k}_{\rm sh}(t) = \frac{1}{2}\int_0^1 |\frac{\partial\mathbf{x}_{\rm sh}}{\partial t}|^2 ds$ and $E^{\rm p}_{\rm sh}(t) = \frac{1}{2}\int_0^1 (\frac{\partial\theta}{\partial t})^2 ds$, respectively. Given the boundary conditions at the sheet edges, Eqs. (7), the first term on the right-hand side of Eq. (B1) vanishes to zero. Therefore, it is left to show that the second term equals the time derivative of the fluid's free energy.

Following Lamb (see p. 9 of Ref. [22]), we recall the following relation between the energy of the fluid and the work done on the fluid's boundaries:

$$\frac{d}{dt}\left[E^{\rm k}_{{\rm f},i}(t) + W_i(t)\right] = \int_0^1 p_i(x_{\rm sh}, y_{\rm sh}, t)\hat{\mathbf{n}}_i\cdot\nabla\phi_i ds, \tag{B2}$$

where $E^{\rm k}_{{\rm f},i}(t) = \frac{1}{2\lambda}\iint_{V_i(t)} |\nabla\phi_i|\rho_i dxdy$ and $W_i(t) = \eta\iint_{V_i(t)}(\ln\rho_i)\rho_i dxdy$ are the kinetic and free energies of the fluid, respectively. In addition, the integral on the right-hand side of Eq. (B2) is taken over the configuration of the sheet. Summing Eq. (B2) over the upper and the lower parts of the chamber, and using the kinematic boundary conditions, Eq. (5), gives

$$\sum_{i={\rm u,d}}\frac{d}{dt}\left[E^{\rm k}_{{\rm f},i}(t) + W_i(t)\right] = \int_0^1 [p_{\rm u}(x_{\rm sh}, y_{\rm sh}, t) - p_{\rm d}(x_{\rm sh}, y_{\rm sh}, t)]\hat{\mathbf{n}}_{\rm d}\cdot\frac{\partial\mathbf{x}_{\rm sh}}{\partial t}ds, \tag{B3}$$

where $\hat{\mathbf{n}}_{\rm d} = -\hat{\mathbf{n}}_{\rm u}$.

Lastly, using Eq. (B3) to replace the last term on the right-hand side of Eq. (B1), and integrating over time, we obtain the conserved quantity

$$E = \frac{1}{2}\int_0^1 \left|\frac{\partial \mathbf{x}_{\mathrm{sh}}}{\partial t}\right|^2 ds + \sum_{i=\mathrm{u,d}} \frac{1}{2\lambda}\iint_{V_i(t)} |\nabla\phi_i|^2 \rho_i dxdy$$
$$+ \frac{1}{2}\int_0^1 \left(\frac{\partial \theta}{\partial s}\right)^2 ds + \sum_{i=\mathrm{u,d}} \eta \iint_{V_i(t)} (\ln \rho_i)\rho_i dxdy, \tag{B4}$$

where the first two terms correspond, respectively, to the kinetic energies of the sheet and the fluid, and the last two terms correspond, respectively, to the potential energy of the sheet and the free energy of the fluid. In the quasistatic analysis, the kinetic energies equal zero, and the density of the fluid in each side of the chamber equals a constant. Therefore, the free energy of the fluid reduces to $W_i(t) = -(\eta L_x L_y/2)\ln V_i$, as appears in Eq. (8).

APPENDIX C: MINIMIZATION OF THE ACTION

In this Appendix, we show that the minimization of the action $\mathcal{S} = \int_0^{\mathcal{T}} \mathcal{L}dt$ yields the equations of motion that we derived in the small-amplitude approximation. For this purpose, we add a small perturbation to the elastic and the hydrodynamic fields, e.g., $y_{\mathrm{sh}}(x,t) \to y_{\mathrm{sh}}(x,t) + \delta y_{\mathrm{sh}}(x,t)$, and expand the action to linear order in the perturbations. This expansion gives

$$\delta\mathcal{S} = \int_0^1 \left[\left(\frac{\partial y_{\mathrm{sh}}}{\partial t} + \frac{1}{\lambda}[\phi_{\mathrm{d}}(x,0,t) - \phi_{\mathrm{u}}(x,0,t)] + tP_{\mathrm{ud}}\right)\delta y_{\mathrm{sh}}\right]_{t=0}^{\mathcal{T}} dx$$
$$+ \frac{1}{\lambda^2\eta}\sum_{i=\mathrm{u,d}}\int_{V_i}\left(\frac{\partial \phi_i}{\partial t}\delta\phi_i\right)_{t=0}^{t=\mathcal{T}} dxdy$$
$$+ \int_0^{\mathcal{T}}\left[-\frac{\partial^2 y_{\mathrm{sh}}}{\partial x^2}\frac{\partial \delta y_{\mathrm{sh}}}{\partial x} + \left(\frac{\partial^3 y_{\mathrm{sh}}}{\partial x^3} + F_x(t)\frac{\partial y_{\mathrm{sh}}}{\partial x}\right)\delta y_{\mathrm{sh}}\right]_{x=0}^{x=1} dt$$
$$- \int_0^{\mathcal{T}}\int_0^1\left(\frac{\partial^2 y_{\mathrm{sh}}}{\partial t^2} + \frac{\partial^4 y_{\mathrm{sh}}}{\partial x^4} + F_x(t)\frac{\partial^2 y_{\mathrm{sh}}}{\partial x^2} + p_{\mathrm{u}}(x,0,t) - p_{\mathrm{d}}(x,0,t)\right)\delta y_{\mathrm{sh}} dxdt$$
$$+ \int_0^{\mathcal{T}}\int_0^1\left(\frac{1}{2}\left(\frac{\partial y_{\mathrm{sh}}}{\partial x}\right)^2 - \Delta\right)\delta F_x dxdt$$
$$+ \int_0^{\mathcal{T}}\int_0^1 [\delta\phi_{\mathrm{d}}(x,0,t) - \delta\phi_{\mathrm{u}}(x,0,t)]\frac{\partial y_{\mathrm{sh}}}{\partial t}dxdt - \frac{1}{\lambda}\sum_{i=\mathrm{u,d}}\int_0^T \oint_{\delta V_i}\nabla\phi_i\cdot\hat{\mathbf{n}}_i\delta\phi_i dsdt$$
$$- \frac{1}{\lambda}\sum_{i=\mathrm{u,d}}\int_0^T\int_{V_i}\left(\frac{1}{\lambda\eta}\frac{\partial^2\phi_i}{\partial t^2} - \nabla^2\phi_i\right)\delta\phi_i dxdydt, \tag{C1}$$

where V_i correspond to the volumes of the chamber above and below the sheet in the small-amplitude approximation, and δV_i are their corresponding perimeters. In the integrals over the perimeters ds and $\hat{\mathbf{n}}_i$ correspond, respectively, to the line element and the normal vector along the contours.

The first and the second lines in Eq. (C1) vanish to zero given the initial conditions. The third line vanishes given the boundary conditions at the sheet edges, Eqs. (7b) and (13b). The fourth and fifth lines resemble the force balance equation, Eq. (10), and the constraint over the lateral displacement, Eq. (9), respectively. Therefore, they both vanish when the equations are satisfied. The last line in Eq. (C1) also vanishes to zero given that the wave equations, Eq. (11b), are satisfied. Therefore, it remains to show that the terms in the sixth line equal zero.

Since at the fluid-chamber interfaces $\nabla\phi_i \perp \hat{\mathbf{n}}_i$ [Eqs. (3)], the contour integrals reduce to two integrals over the configuration of the sheet. Therefore, we obtain

$$\delta\mathcal{S} = \frac{1}{\lambda}\int_0^T \int_0^1 \left[\left(\frac{\partial y_{\rm sh}}{\partial t} - \left(\frac{\partial \phi_{\rm d}}{\partial y}\right)_{y=0}\right)\delta\phi_{\rm d}(x,0,t) - \left(\frac{\partial y_{\rm sh}}{\partial t} - \left(\frac{\partial \phi_{\rm u}}{\partial y}\right)_{y=0}\right)\delta\phi_{\rm u}(x,0,t)\right] dxdt. \tag{C2}$$

These two terms equal zero given that the kinematic boundary conditions, Eq. (13a), are satisfied. This completes the proof that the small-amplitude model emanates from the minimization of the action.

APPENDIX D: MODES OF VIBRATIONS IN RECTANGULAR CHAMBER

When the sheet remains flat ($\Delta = 0$), there is no feedback between the upper and lower sections of the chamber, and the fluid in each part vibrates independently. Therefore, to analyze the modes of vibration, it is sufficient to solve the wave equation, along with no-penetration conditions on the chamber's walls, for just one section of the chamber. These boundary conditions are all satisfied when the potential functions are given by

$$\phi_i(x,y,t) = \sum_{m_x=0}^{\infty}\sum_{m_y=0}^{\infty} a^i_{m_x m_y}(t)\cos(\pi m_x x)\cos\left(\frac{2\pi m_y}{L_y}y\right), \tag{D1}$$

where $a^i_{m_x m_y}(t)$ are time-dependent functions. To obtain the frequencies of vibration, we expand the modal amplitudes around their zero base solutions, $a^i_{m_x m_y}(t) = \epsilon \bar{a}^i_m e^{i\omega t}$, and substitute these expansions into the wave equation. The solution of this equation implies that all modes are decoupled and that their corresponding frequencies are given by

$$\omega = \pi(\lambda\eta)^{1/2}\left[m_x^2 + \left(\frac{2m_y}{L_y}\right)^2\right]^{1/2}. \tag{D2}$$

It should be noted that the dependence of these frequencies on the mass ratio λ and the thermal-to-bending energy ratio η arises from our normalization of time and length with respect to the sheet's properties. When dimensions are reintroduced into the formulation, we find that the frequencies scale as $(RT/L^2)^{1/2}$, without any dependence on the characteristics of the sheet (here, L corresponds to the horizontal dimension of the chamber). Nonetheless, for comparison with the more general case, where the sheet and the fluid interact, we maintain the normalization of the main text.

The lowest frequency in Eq. (D2) depends on the vertical dimension of the chamber and is given by

$$L_y < 2: \ \omega = \pi(\lambda\eta)^{1/2} \quad (m_x = 1 \text{ and } m_y = 0), \tag{D3a}$$

$$L_y > 2: \ \omega = \frac{2\pi}{L_y}(\lambda\eta)^{1/2} \quad (m_x = 0 \text{ and } m_y = 1). \tag{D3b}$$

The eigenfunction that corresponds to $L_y < 2$ yields an oscillatory motion of the fluid in the x direction, i.e., $\phi_i \sim \cos(\pi x)$, while the eigenfunction that corresponds to $L_y > 2$ yields an oscillatory motion of the fluid in the y direction, i.e., $\phi_i \sim \cos(2\pi y/L_y)$. In the main text, we showed that in the limit $\eta/\eta_\star \ll 1$ the frequency of the symmetric branch, Eq. (25a), coincides with Eq. (D3a). However, it should be kept in mind that when the normalized vertical dimension of the chamber exceeds a length of 2, the lowest frequency is obtained from Eq. (D3b) at some finite value of η.

APPENDIX E: THE LOWEST FREQUENCY OF VIBRATIONS IN AN INCOMPRESSIBLE FLUID

In this Appendix, we assume that the chamber is filled with an incompressible fluid and we derive the lowest frequency of vibration when the base solution of the sheet is either the first or the second mode of buckling. Our objectives in this derivation are to demonstrate that (i) the coefficient in Eq. (25b) coincides with the lowest frequency around the first mode in the case of an incompressible fluid, and (ii) in the limit $\eta/\eta_\star \gg 1$, the lowest frequency around the second mode, Eq. (30), coincides with its counterpart in an incompressible fluid.

To this end, we employ the small-amplitude approximation and adjust the Lagrangian (14) to account for an incompressible fluid. This adjustment requires us to eliminate the equation of state (1a) from the formulation and to add a constraint on the volumes of the fluids above and below the sheet. These modifications result in

$$\begin{aligned}\mathcal{L} = \int_0^1 \Bigg[&\frac{1}{2}\left(\frac{\partial y_{\text{sh}}}{\partial t}\right)^2 - \frac{1}{2}\left(\frac{\partial^2 y_{\text{sh}}}{\partial x^2}\right)^2 \\ &+ F_x(t)\left(\frac{1}{2}\left(\frac{\partial y_{\text{sh}}}{\partial x}\right)^2 - \Delta\right) + \frac{1}{\lambda}[\phi_{\text{d}}(x,0,t) - \phi_{\text{u}}(x,0,t)]\frac{\partial y_{\text{sh}}}{\partial t}\Bigg]dx \\ &+ P_{\text{ud}}(t)\left(\int_0^1 y_{\text{sh}}dx + \frac{L_xL_y}{2} - V_{\text{d}}\right) - \frac{1}{2\lambda}\int_0^{\frac{L_y}{2}}\int_0^1 |\nabla\phi_{\text{u}}|^2 dxdy - \frac{1}{2\lambda}\int_{-\frac{L_y}{2}}^0\int_0^1 |\nabla\phi_{\text{d}}|^2 dxdy.\end{aligned} \tag{E1}$$

Importantly, here $P_{\text{ud}}(t)$ is a Lagrange multiplier that enforces the constraint of the constant volume [13]. It does not satisfy the equation of state of the main text, Eq. (12).

In addition, we assume the following modal expansions of the fluid's potential functions:

$$\phi_i(x,y,t) = \sum_{m=1}^{N-1} a_m^i(t)\cos(\pi m x)\cosh\left[\pi m\left(y \pm \frac{L_y}{2}\right)\right], \tag{E2}$$

where the $\pm$ signs correspond to the lower and the upper parts of the chamber, respectively. These expansions automatically satisfy the continuity equations of an incompressible fluid ($\nabla^2\phi_i = 0$) and the boundary conditions at the fluid-chamber interfaces, Eqs. (3). Note that, in contrast to the compressible fluid scenario, the wave numbers in the x and y directions are identical, and in the y direction the wave is always localized around the area of the sheet. The Fourier expansion of the sheet remains similar to that given by Eq. (16), which satisfies the hinged boundary conditions.

In the next step, we substitute Eqs. (E2) and (16) into the Lagrangian, Eq. (E1), and integrate with respect to the spatial coordinates. Thereafter, we minimize the Lagrangian with respect to $a_m^i(t)$ and express the coefficients in terms of $A_n(t)$. Substituting $a_m^i(t)$ back into the Lagrangian gives

$$\mathcal{L} = T_{nk}\frac{dA_n}{dt}\frac{dA_k}{dt} - V_{nk}A_nA_k + F_x(t)C_{nk}A_nA_k + P_{\text{ud}}(t)A_nW_1(n,0) - F_x(t)\Delta + P_{\text{ud}}(t)\left(\frac{L_xL_y}{2} - V_{\text{d}}\right), \tag{E3}$$

where in this Appendix Einstein's summation rule is implied for repeated indices, and we define the following symmetric matrices:

$$T_{nk} = \frac{1}{4}\delta_{nk} + \sum_{m=1}^{N-1}\frac{2}{\pi m\lambda}\coth\left(\frac{\pi m L_y}{2}\right)W_1(k,m)W_1(n,m), \tag{E4a}$$

$$V_{nk} = \frac{\pi^4}{4}n^2k^2\delta_{nk}, \quad C_{nk} = \frac{\pi^2}{4}nk\delta_{nk}, \tag{E4b}$$

where δ_{nk} is the Kronecker delta, and $W_1(n,m) = \frac{n}{\pi}\frac{1-(-1)^{n+m}}{n^2-m^2}$ for $n \neq m$ and zero otherwise.

To perform the linear stability analysis, we expand the modal amplitude, the lateral compression, and the pressure difference around their base solutions:

$$A_n(t) = A_n(0) + \epsilon e^{i\omega t}\bar{A}_n, \quad n = 1, 2, 3, \dots, \tag{E5a}$$

$$F_x(t) = F_x(0) + \epsilon e^{i\omega t}\bar{F}_x, \tag{E5b}$$

$$P_{\mathrm{ud}}(t) = P_{\mathrm{ud}}(0) + \epsilon e^{i\omega t}\bar{P}_{\mathrm{ud}}, \tag{E5c}$$

where we use the same notation as in Sec. IV to define the base solution and the corresponding perturbation around this shape. Subsequently, we minimize the Lagrangian (E3) with respect to $A_n(t)$, $F_x(t)$, and $P_{\mathrm{ud}}(t)$ and expand the equations in powers of ϵ. To leading order, order ϵ^0, the equations read

$$(V_{nk} - F_x(0)C_{nk})A_k(0) = \frac{P_{\mathrm{ud}}(0)}{2}W_1(n, 0), \quad n = 1, 2, 3, \dots, \tag{E6a}$$

$$C_{nk}A_n(0)A_k(0) = \Delta, \tag{E6b}$$

$$A_n(0)W_1(n, 0) = V_{\mathrm{d}} - \frac{L_xL_y}{2}, \tag{E6c}$$

and to the subleading order, order ϵ, the equations are

$$[-\omega^2T_{nk} + V_{nk} - C_{nk}F_x(0)]\bar{A}_k - C_{nk}A_k(0)\bar{F}_x = \frac{\bar{P}_{\mathrm{ud}}}{2}W_1(n, 0), \quad n = 1, \dots, N, \tag{E7a}$$

$$C_{nk}A_k(0)\bar{A}_n = 0, \tag{E7b}$$

$$\bar{A}_nW_1(n, 0) = 0. \tag{E7c}$$

This concludes the derivation of the equations. In summary, to determine the lowest frequency of vibrations, we first solve Eq. (E6) for the base solution $A_n(0), F_x(0), P_{\mathrm{ud}}(0)$. Subsequently, we substitute this solution into the equations of the subleading order, Eqs. (E7), and solve them for the frequency ω. As higher modes of the sheet are included in the solution, the frequency approaches its exact value more closely. However, the mathematical complexity of the solution also increases. In the next sections, we obtain the frequency of the vibrations around the first and second modes of buckling by using the minimal number of modes.

1. The lowest frequency around the first mode

To determine the frequency of vibrations around the first mode of buckling, we employ the two-mode approximation. This choice arises from the observation that, when the sheet accommodates a symmetric configuration, it is disturbed primarily by an asymmetric eigenfunction. In this approximation, the downwards volume is given by $V_{\mathrm{d}} = \frac{4\sqrt{\Delta}}{\pi^2} + \frac{L_xL_y}{2}$ [13], and the solution of Eq. (E6) is given by

$$A_1(0) = \frac{2\sqrt{\Delta}}{\pi}, \quad F_x(0) = \pi^2, \quad P_{\mathrm{ud}}(0) = 0, \tag{E8}$$

where $A_2(0) = 0$. When this base solution is substituted into the equations at the subleading order, Eqs. (E7), we find that $\bar{A}_1 = \bar{F}_x = \bar{P}_{\mathrm{ud}} = 0$ and that all the equations are satisfied when

$$\omega \equiv \omega_{\mathrm{in}}^{\mathrm{sym}} = \frac{2\sqrt{3}\pi^2}{\sqrt{1 + \frac{128\coth(\pi L_y/2)}{9\pi^3\lambda}}}. \tag{E9}$$

This solution coincides with Eq. (25b) when $\eta = 0$. Its corresponding eigenfunction yields a vortexlike patterned flow that is localized in the y direction, as described in Fig. 4(b).

2. The lowest frequency around the second mode

When the sheet accommodates the second mode of buckling, the volume difference in the chamber equals zero and $V_\mathrm{d} = L_x L_y/2$. This requirement, which holds throughout the dynamic evolution, prompts us to relax the two-mode approximation. The relaxation is necessary because the two-mode approximation implies that when the base solution is asymmetric, it is perturbed primarily by the symmetric mode, which alters the volumes in the chamber. Mathematically, it can readily be verified that the two-mode approximation consistently yields the trivial solution $\bar{A}_1 = \bar{A}_2 = 0$.

As we now show, the minimum number of modes required to obtain a nontrivial solution is $N = 3$. In this case, the solution of Eq. (E6) yields $A_1(0) = A_3(0) = 0$ and all the equations are satisfied when

$$A_2(0) = \frac{\sqrt{\Delta}}{\pi}, \quad F_x(0) = 4\pi^2, \quad P_\mathrm{ud}(0) = 0. \tag{E10}$$

When this solution is substituted in the subleading order, Eqs. (E7), we find that $\bar{A}_2 = \bar{F}_x = 0$, and that the eigenfunction comprises of a linear combination of $\bar{A}_1$ and $\bar{A}_3$ that maintains a fixed volume difference in the chamber [see Eq. (E7c)]. The latter equations have a nontrivial solution when

$$\omega \equiv \omega_\mathrm{in}^\mathrm{asy} = \frac{\sqrt{201/5}\pi^2}{\sqrt{1 + \frac{8192\coth(\pi L_y)}{1125\pi^3\lambda}}}, \tag{E11}$$

as given in Eq. (30). As shown in Fig. 7(a), this solution approximates the frequency in the asymmetric branch in the limit $\eta/\eta_\star \gg 1$. Its corresponding eigenfunction induces two counterrotating vortices that are localized in the y direction [see Fig. 7(c)].

[1] I. Simon, N. Bârsan, M. Bauer, and U. Weimar, Micromachined metal oxide gas sensors: Opportunities to improve sensor performance, Sens. Actuators B **73**, 1 (2001).

[2] H. Tuller and R. Mlcak, Photo-assisted silicon micromachining: Opportunities for chemical sensing, Sens. Actuators B **35**, 255 (1996), Proceedings of the Sixth International Meeting on Chemical Sensors.

[3] S. Schneider, D. Gruner, A. Richter, and P. Loskill, Membrane integration into PDMS-free microfluidic platforms for organ-on-chip and analytical chemistry applications, Lab Chip **21**, 1866 (2021).

[4] A. O. Stucki, J. D. Stucki, S. R. R. Hall, M. Felder, Y. Mermoud, R. A. Schmid, T. Geiser, and O. T. Guenat, A lung-on-a-chip array with an integrated bio-inspired respiration mechanism, Lab Chip **15**, 1302 (2015).

[5] H. Kim, Q. Zhou, D. Kim, and I.-K. Oh, Flow-induced snap-through triboelectric nanogenerator, Nano Energy **68**, 104379 (2020).

[6] H. Kim, M. Lahooti, J. Kim, and D. Kim, Flow-induced periodic snap-through dynamics, J. Fluid Mech. **913**, A52 (2021).

[7] S. Qi, M. Oudich, Y. Li, and B. Assouar, Acoustic energy harvesting based on a planar acoustic metamaterial, Appl. Phys. Lett. **108**, 263501 (2016).

[8] X. Fan, J. Chen, J. Yang, P. Bai, Z. Li, and Z. L. Wang, Ultrathin, rollable, paper-based triboelectric nanogenerator for acoustic energy harvesting and self-powered sound recording, ACS Nano **9**, 4236 (2015).

[9] L.-Q. Tao, H. Tian, Y. Liu, Z.-Y. Ju, Y. Pang, Y.-Q. Chen, D.-Y. Wang, X.-G. Tian, J.-C. Yan, N.-Q. Deng, Y. Yang, and T.-L. Ren, An intelligent artificial throat with sound-sensing ability based on laser induced graphene, Nat. Commun. **8**, 14579 (2017).

[10] O. Oshri, Asymptotic softness of a laterally confined sheet in a pressurized chamber, Phys. Rev. E **104**, 055005 (2021).

[11] O. Oshri, Modeling the behavior of an extensible sheet in a pressurized chamber, J. Elast. **153**, 549 (2023).

[12] K. Goncharuk, Y. Feldman, and O. Oshri, Fluttering-induced flow in a closed chamber, J. Fluid Mech. **976**, A15 (2023).

[13] O. Oshri, Volume-constrained deformation of a thin sheet as a route to harvest elastic energy, Phys. Rev. E **103**, 033001 (2021).

[14] D. J. Preston, H. J. Jiang, V. Sanchez, P. Rothemund, J. Rawson, M. P. Nemitz, W.-K. Lee, Z. Suo, C. J. Walsh, and G. M. Whitesides, A soft ring oscillator, Sci. Rob. **4**, eaaw5496 (2019).

[15] G. Arena, R. M. J. Groh, A. Brinkmeyer, R. Theunissen, P. M. Weaver, and A. Pirrera, Adaptive compliant structures for flow regulation, Proc. R. Soc. A **473**, 20170334 (2017).

[16] B. McCarthy, G. Adams, N. McGruer, and D. Potter, A dynamic model, including contact bounce, of an electrostatically actuated microswitch, J. Microelectromech. Syst. **11**, 276 (2002).

[17] P. N. Nge, C. I. Rogers, and A. T. Woolley, Advances in microfluidic materials, functions, integration, and applications, Chem. Rev. **113**, 2550 (2013).

[18] S.-H. Chiu and C.-H. Liu, An air-bubble-actuated micropump for on-chip blood transportation, Lab Chip **9**, 1524 (2009).

[19] Y.-N. Wang and L.-M. Fu, Micropumps and biomedical applications—a review, Microelectron. Eng. **195**, 121 (2018).

[20] M. Safaei, H. A. Sodano, and S. R. Anton, A review of energy harvesting using piezoelectric materials: State-of-the-art a decade later (2008–2018), Smart Mater. Struct. **28**, 113001 (2019).

[21] C. Wei and X. Jing, A comprehensive review on vibration energy harvesting: Modelling and realization, Renewable Sustainable Energy Rev. **74**, 1 (2017).

[22] H. Lamb, *Hydrodynamics* (Dover, New York, 1945).

[23] O. Oshri, K. Goncharuk, and Y. Feldman, Snap-induced flow in a closed channel, J. Fluid Mech. **986**, A12 (2024).

[24] We divided the equation by $\cos(q_1 L_y/2)$ because, in cases where this term equals zero, it always leads to a frequency greater than the smallest solution of Eq. (24).

[25] A. Pandey, D. E. Moulton, D. Vella, and D. P. Holmes, Dynamics of snapping beams and jumping poppers, Europhys. Lett. **105**, 24001 (2014).

[26] The points at which the eigenfunction equal zero are given by the first root of the equations $\tan(\pi x) = \pm\sqrt{2}$.